Tracking changes in the co-eruptive seismic tremor associated with magma degassing at Piton de la Fournaise volcano

Cyril Journeau [a,b,*], Nikolai M. Shapiro [a], Aline Peltier [c,d], Valérie Ferrazzini [c,d], Jean Soubestre [a,e], Zacharie Duputel [c,d], Andrea Di Muro [f], Claude Jaupart [c], Diego Coppola [g]

[a] Univ. Grenoble Alpes, Univ. Savoie Mont Blanc, CNRS, IRD, Univ. Gustave Eiffel, ISTerre, 38000 Grenoble, France
[b] Earth Sciences Department, University of Oregon, Eugene, OR, USA
[c] Université de Paris, Institut de Physique du Globe de Paris (IPGP), CNRS (UMR 7154), Paris, France
[d] Observatoire Volcanologique du Piton de la Fournaise, Institut de Physique du Globe de Paris (IPGP), La Plaine des Cafres, France
[e] Icelandic Meteorological Office, Reykjavik, Iceland
[f] Laboratoire de Géologie de Lyon : Terre, Planètes, Environnement, CNRS (UMR 5276), Ecole Normale Supérieure de Lyon, Université Claude Bernard Lyon 1, Villeurbanne, France
[g] Department of Earth Sciences, University of Torino, Torino, Italy

ARTICLE INFO

ABSTRACT

Volcanic eruptions in basaltic systems represent the most frequent expression of volcanic activity in the World, whose surface manifestations range from effusive lava flows to more explosive events. Their eruptive dynamics and style are largely controlled by the degassing of magma. In this study, we analyze seismic tremors recorded during 23 eruptions that occurred at Piton de la Fournaise volcano (La Réunion, France) during 2014–2021 and show that their properties are strongly linked to the magma degassing. We apply the network covariance matrix method to build a catalog of tremor sources associated with all 23 eruptions, to measure their time-frequency properties, and to locate their sources. We then conduct a multi-disciplinary analysis by comparing the seismic tremor observations with images of the eruptive sites, lava flow rate measurements, impulsive earthquakes, as well as deformation and magma composition data. The tremor depth distribution is found to be well correlated with magma gas content, indicating that the tremor generating mechanism is largely controlled by the shallow magma degassing under the eruptive site. The resulting seismic tremor signals analysis enable to track changes in degassing regimes and associated eruptive styles at the surface, thus improving monitoring and knowledge of the eruptive dynamics of the studied volcano.

1. Introduction

Basaltic systems exist in all types of geodynamic settings (hot spot, rift zone, subduction zones) (Walker, 1993) and their eruptions are the most common manifestation of surface volcanic activity on Earth (Houghton and Gonnermann, 2008). The main driver of these eruptions is the formation of gaseous phase during the exsolution of the volatile elements dissolved in liquid magma (dominantly H_2O and CO_2) when it ascents toward the surface and decompresses through nucleation of gas bubbles (Sparks, 2003; Vergniolle and Gaudemer, 2015).

This degassing in low-viscosity basaltic systems can give rise to several flow regimes in volcanic conduits (Jaupart and Vergniolle, 1988; Gonnermann and Manga, 2013), generating a wide range of eruptive styles going from effusive lava flows to mild explosive Strombolian explosions and Hawaiian fountaining and more rarely intensively explosive Vulcanian eruptions. The corresponding gas-liquid flow dynamic and possible transitions between regimes depend on several parameters, including physico-chemical magma properties (temperature, pressure, composition, viscosity, initial content of dissolved volatiles elements), conduit geometry (James et al., 2004), conduit roughness, and gas flow rate (Spina et al., 2019).

Therefore, in order to better understand the mechanisms involved and to better apprehend the volcano behavior and its potential evolution toward phases of unrest, we need to monitor active basaltic systems by acquiring multi-disciplinary data and cross-referencing them.

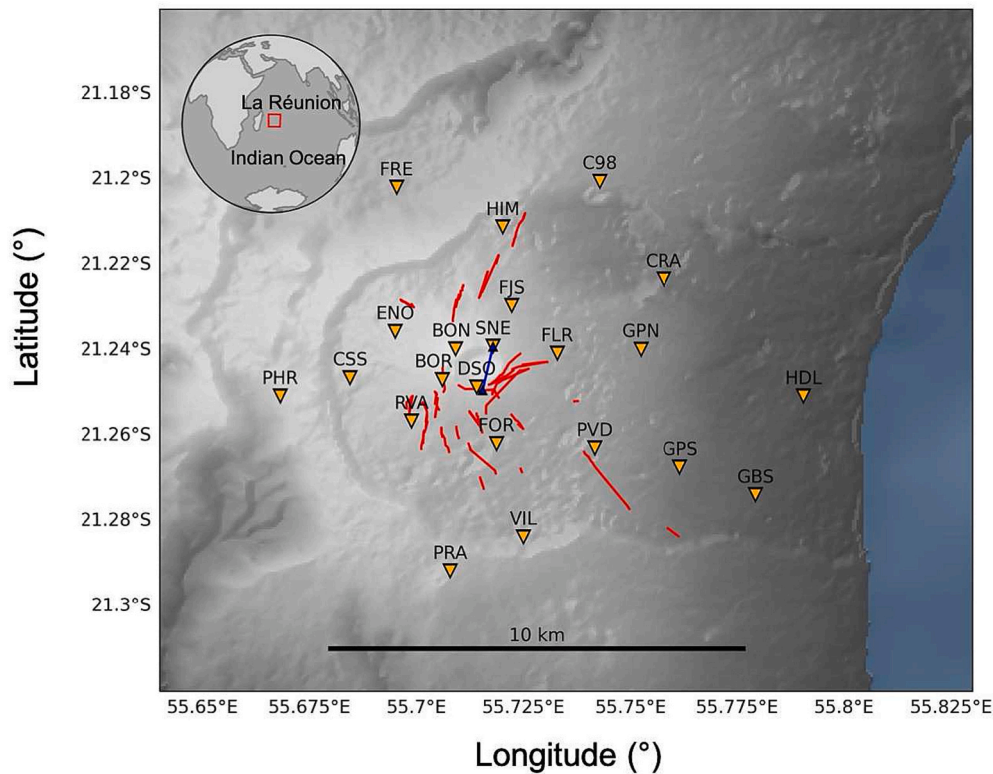Among several tools, analysis of seismovolcanic signals has proven

Fig. 1. Grey shaded relief map of the Piton de la Fournaise volcano, located on the southeastern part of La Réunion island. The top left inset shows the location of La Réunion island in the Indian Ocean. Seismic stations used in this study are represented with orange inverted triangles. The blue line connecting the blue triangles correspond to the baseline computation between SNEG-DSRG GNSS stations. Red lines stand for the position of the eruptive fissures corresponding to all eruptions analyzed in this study. (For interpretation of the references to colour in this figure legend, the reader is referred to the web version of this article.)

very efficient for improving our understanding of volcanic systems and to infer their complex dynamics (Chouet and Matoza, 2013). In particular, long-period (LP) seismicity is thought to be associated with the gas-liquid dynamics and their interaction with solid rock. This category of seismicity encompasses both continuous tremor and impulsive LP events and is characterized by frequency content between 0.5 and 5 Hz (Chouet, 1996). Physical mechanisms generating volcanic tremors are not yet completely understood and they can vary depending on the volcanic system and depth of source activation (Konstantinou and Schlindwein, 2003; Chouet and Matoza, 2013). However, most of existing source models involve pressure fluctuations at the origin of the sustained long-period oscillations characterizing tremor signals. In particular, degassing is often invoked as a possible source for the generation of the LP seismicity in different volcanic systems, from their deep roots, for example at Klyuchevskoy (Melnik et al., 2020), to their shallow parts, for example at Kilauea (Chouet and Dawson, 2011) or at Etna (Patanè et al., 2008; De Barros et al., 2011).

In this study, we focus on recent eruptions of the Piton de la Fournaise (PdF) volcano and investigate the co-eruptive seismic tremors and the associated degassing dynamics. To better understand the origin of the volcanic tremor at PdF and to extract information on the dynamics of its eruptions, we analyze in detail the continuous data recorded by its dense seismic network (Fig. 1). We then compare the outputs with others available multi-disciplinary eruptive parameters. In particular, we want to analyze spatial, spectral and temporal patterns in tremor data that may indicate change in the gas-liquid dynamics regime and to investigate their relationship with the lava discharge rate at the vent, petrological information on lava products, pictures of the eruptive cone, deformation of the volcanic edifice and associated co-eruptive seismicity.

PdF is an ideal natural laboratory for testing these ideas, being one of the most active, with more than two eruptions per year in average (Roult

et al., 2012; Staudacher et al., 2016; Chevrel et al., 2021), and most densely instrumented volcano in the World, with more than 100 geophysical and geochemical sensors distributed on the island. Each PdF eruption is associated with a co-eruptive seismic tremor and thanks to good instrument maintenance, all these eruptive seismic signatures have been recorded with a dense seismic network in the vicinity of the volcano (from 16 to 20 seismic stations depending on data availability, within a 15 km diameter circle) for the last 23 eruptions that occurred in the 2014–2021 time period. The resulting large tremor database contains thus a wealth of important information and requires advanced network-based methods for its exploration.

In section 2, we introduce the PdF eruptive dynamics with associated degassing and seismic tremor patterns. Then, we present in section 3 our methodological approach allowing to infer the spatial, temporal and spectral properties of the seismic tremor and to compare our outputs in a multi-disciplinary dataset. The obtained results are presented in section 4 and finally discussed in section 5.

2. Regional settings: the Piton de la Fournaise eruptive dynamics and associated eruptive tremors

2.1. Piton de la Fournaise volcanism origin and current dynamics

La Réunion is a volcanic island located on the African plate, southwest of the Indian ocean in the Marscarene Basin (Fig. 1). Based on dating and geodynamic reconstruction, its volcanism is thought to have a hot spot origin, being generated by the same mantle plume that produced the Deccan Trapp about 65 Ma ago (Courtillot et al., 1986). The head of this mantle plume would have passed beneath La Réunion about 5 Ma (Bonneville, 1990), and the plume conduit would be now located at 100–200 km north of the island (Barruol and Fontaine, 2013). Tsekhmistrenko et al. (2021) present a high resolution body-wave

tomography of the whole mantle column beneath the western Indian Ocean providing a more complex view of the plume beneath La Réunion. Their model reveals that the mantle upwellings present a tree-like structure and show considerable tilt in the lower mantle instead of being near-vertical, splitting into branches near the surface. Wamba et al. (2021, 2023) derived a multi-mode waveform shear wave tomography revealing that the hotspot feeding source is anchored at the core-mantle boundary, with a deep mantle plumbing system including alternating vertical conduits and horizontal ponding zones.

The Piton de la Fournaise volcano is an intraplate shield basaltic volcano of Hawaiian type located in the southeastern part of the island. It is 2631 m high and active since about 530 ka. Throughout its existence, this volcano has been marked by the formation of successive concentric calderas, the latest being the Enclos Fouqué, formed about 4500 years ago (Bachèlery, 1981), in which there is a summit cone of 400 m high and 3 km wide at its base.

The eruptive activity of PdF can be described as cycles with periods of high activity with an average of two eruptions per year, separated by periods of three to six years without activity. After a break of more than five years between 1992 and 1998, the volcano has become very active again. There was then a 3.5 year break between 2010 and 2014, with a resumption of activity in June 2014. The volcano is still in an active period at the time of writing this paper and the last eruption considered in this analysis is that of December 2021–January 2022. For the 23 eruptions that occurred during our study period (2014–2021), the average rate of magma released is 0.63 m^3/s.

During inter-eruptive periods, one of the long-term precursor signals of an eruption is the inflation of the volcanic edifice seen by the GNSS deformation sensors. This inflation is interpreted as the expansion of the shallow magmatic reservoir located at 1500–2500 m below PdF summit (Peltier et al., 2005, 2008) due to a replenishment from the deep system. Such a deep recharge can be resolved over ten days thanks to the inversion of GNSS data (Beauducel et al., 2020). Some precursors are also visible in seismic velocity changes measured by cross-correlation of ambient noise. Indeed, several studies have been conducted at PdF, showing decreases in seismic velocity correlated with edifice inflation, likely linked to some magma pressure buildup before an eruption. (Brenguier et al., 2008; Duputel et al., 2009; Rivet et al., 2014; Sens-Schönfelder et al., 2014; Rivet et al., 2015).

The short-term precursor signals are the triggering of a seismic crisis composed of hundreds of volcano-tectonic earthquakes (VTs) and a strong increase in the rate of deformation of the volcano (Roult et al., 2012). The resulting seismic swarm is interpreted as the activation of a ring-fault portion located above the shallow magma reservoir while magma starts its upward propagation (Duputel et al., 2019).

Magma is then transported via the propagation of dykes or sills through the shallow system until the fissure opening at the surface marks the beginning of an eruption, either on the summit or on one of the flanks of the volcano (Peltier et al., 2005; Smittarello et al., 2019; Dumont et al., 2022). This propagation phase is marked by a decrease in the number of observed VTs and it is generally accompanied by a higher frequency micro-seismicity. Locating this micro-seismicity tracks the progress of the magma toward the eruptive site (Taisne et al., 2011; De Barros et al., 2013; Journeau et al., 2020).

Melt and fluid inclusion studies show that PdF magmas undergo extensive CO_2 degassing at mantle level and that water and SO_2 exsolution dominate degassing at shallow crustal level, halogens being released only at very shallow level (Di Muro et al., 2016). On average, PdF magmas contain low to moderate volatile contents, due to their multistep ascent and degassing at shallow depth (Verdurme et al., 2022). Magmas emitted after long phases of quiescence like in June 2014 have experienced extensive degassing and crystallization at shallow level (Gurioli et al., 2018).

As generally observed at basaltic volcanoes, PdF eruptions start with opening of hundred-meters-long eruptive fissures associated with lava fountaining. After a few hours, eruptions focalize to a single vent,

generally at the lowest point of the eruptive fissures (Fukushima et al., 2010). At this stage, magma degassing typically changes from a Hawaiian to a Strombolian regime (Thivet et al., 2020a). Such activity can either persist a few hours/days or a few weeks/months when associated with magma re-feeding phases.

Eruptions typically end when the overpressure driving the magma/gas is exhausted, with no further lava emission at the surface, a process commonly accompanied with a transition toward an intermittent degassing regime. This last phase is often reported in the IPGP-OVPF volcanological bulletins (https://www.ipgp.fr/en/observatory-releases-and-bulletins/) as seismic sequences of "gas-pistons" marking the end of the eruptions, the last gas puffs being seen in the seismic records as discrete tremor bursts.

Gas pistoning is a style of degassing that was first described by Swanson et al. (1979) at Kilauea volcano during the 1969–1971 Mauna Ulu eruption. Gas acts as a piston promoting the cyclic rise of the lava level in a conduit until bubbling and gas-jetting are observed, followed by an abrupt fall of the lava column. Two different source mechanisms can explained such gas-piston activity: a cyclic effusion–gas-jetting–drain-back model and a foam layer collapse mechanism (Marchetti and Harris, 2008). In the first model, the lava column is pushed upwards due to the build-up of gas beneath a relatively impermeable magma layer, until lava spreads on the surface, decreasing pressure on top of the gas layer and thus inducing gas release by gas-jetting (Swanson et al., 1979; Johnson et al., 2005). The second model is based on the accumulation of gas bubbles at magmatic chamber roof or conduit constriction, forming a foam that collapses when reaching a critical thickness. This foam collapse generates a rising gas slug in the conduit that bursts at the free surface and release the over-pressurized gas (Jaupart and Vergniolle, 1988, 1989; Vergniolle and Jaupart, 1990).

Short-period seismic records of gas-pistoning at Kilauea volcano have been analyzed by Chouet and Shaw (1991); Ferrazzini et al. (1991); Goldstein and Chouet (1994). A clear link has been established between those seismic signals and vigorous degassing episodes, with the paroxysmal gas release corresponding to the maximum observed seismic amplitudes. More recently, Chouet and Dawson (2015) analyzed broadband seismic records of Kilauea gas-pistoning activity which is simulated with a foam growth and collapse model.

More rarely, the ending phases of Piton de la Fournaise eruptions are characterized by "effusive paroxysms", with an intensification of the eruptive activity at the surface and a return of the lava fountains followed by a very abrupt end within a few minutes (Coppola et al., 2017; Verdurme et al., 2022).

2.2. Co-eruptive seismic tremors

The PdF eruptions thus exhibit a wide range of eruptive styles associated with different degassing regimes with a more or less complex time evolution. All these eruptions are recorded by the PdF seismic network and corresponding seismic tremor signal can be seen as the eruptive seismic signature. Given the spatially dense seismic network and the high temporal resolution sampling compared to other observatory data, the seismic tremor database is ideal for monitoring eruptions, catching fine patterns of their dynamics, and inferring the underlying magmatic processes at play.

It is one of the first times that we can study the seismic records of so many eruptions at a single volcano with a stable and dense network. It is important to scan long time series of data including several eruptions to investigate the different observed patterns and to have a broader vision regarding the different PdF eruptive manifestations and mechanisms governing their dynamics.

Using a method based on measuring the tremor amplitude at different stations of a network, Battaglia and Aki (2003); Battaglia et al. (2005b) located sources of several co-eruptive tremors at the PdF for eruptions between 1998 and 2000. They found a shallow source correlating with the eruptive vents position for frequencies above 1.5 Hz and

suggested that lower tremor frequencies could be related to deeper processes. Using a different approach based on seismic network cross-correlations, Journeau et al. (2020) located tremor sources corresponding to the three eruptions of 2010, the first ones recorded by a dense seismic network of 21 stations at PdF. The resulting locations are thus more precise and show a very shallow position correlating perfectly with that of the corresponding eruptive site. In this study, we systematically locate all co-eruptive tremor sources associated with the following 23 eruptions between 2014 and 2021 and represent the results in the section 4.

As it is difficult to deduce a unique physical tremor mechanism and to interpret its signal fluctuations, it is essential to ground our observations in a larger database including different disciplines, allowing them to be put into perspective and to have several points of view on the eruptive processes. This knowledge acquired by cross-referencing different information can ultimately be re-used at volcano observatories in real-time, to read more easily the seismic tremor data and translate them into physical eruptive parameters (physico-chemical magma properties, size of the dyke/conduits, output lava flow, etc), allowing a quantitative monitoring of the PdF eruptive dynamics evolution.

Investigating relations between seismic tremor amplitude and lava discharge rate can be useful to better apprehend the mechanism linking them. Power law scaling relations with different power indices have been proposed based on various data sets and are reviewed by Ichihara (2016). These relations have been extensively studied at PdF (Battaglia et al., 2005a; Coppola et al., 2009; Hibert et al., 2015). It is suggested that these relations depend on the style of activity and that tremor may be associated with both frictional dissipation of the flow inside the conduit and rate of burst and size of bubbles. In the continuity of these works, we also report some relationships between lava discharge rate, tremor amplitude and frequency content for a certain number of eruptions occurring in the 2014–2021 time period.

3. Data and methods

3.1. Seismic data analysis

We based our analysis on the seismic network covariance matrix approach allowing an ensemble representation of inter-stations cross-correlations as suggested by Seydoux et al. (2016a, 2016b, 2017). We use the vertical component records of the seismic network stations in the vicinity of PdF (PF network, https://doi.org/10.18715/reunion.PF). The data are stored in 24-h-long time series in mseed format and downsampled from 100 to 20 samples per second. We apply demeaning, linear detrending, and bandpass filtering between 1 and 10 Hz. Then, some spectral whitening is applied. This data analysis was performed using the CovSeisNet software (available at: https://github.com/covseisnet/covseisnet).

We first describe the covariance matrix approach that is well suited for the analysis of continuous tremor-like signals. We then present a template-matching approach to detect change from continuous to discrete tremor. Those two methods are applied to the 23 eruptions of our tremor catalog. We finally applied a template-matching and relocation method to the long-duration July–August 2017 eruption in order to better characterize its corresponding co-eruptive seismicity composed of different impulsive earthquakes signals.

3.1.1. Detection, location, classification and characterization of tremors based on the covariance matrix analysis

3.1.1.1. Covariance matrix and its eigenvalues: distinguishing seismic tremor from seismic ambient noise. According to Seydoux et al. (2016a), the covariance matrix $\mathbf{C}(f)$ is estimated in an averaging time window of length Δt, from the time average of the Fourier cross-spectra matrices

computed over a set of M overlapping subwindows of length δt, such as:

$$\mathbf{C}(f) = \langle \mathbf{u}(f)\mathbf{u}^{\dagger}(f) \rangle_{\Delta t} = \frac{1}{M}\sum_{m=1}^{M}\mathbf{u}_m(f)\mathbf{u}_m^{\dagger}(f), \qquad (1)$$

with $\mathbf{u}_m(f)$ the data Fourier spectra vector in the subwindow m for the entire network.

We applied this calculation on consecutive averaging windows over the whole 2014–2021 time period, setting $M = 20$, $\delta t = 60s$ and the overlapping ratio to 50%, to obtain 10-min-long time windows.

Once estimated, this matrix can be decomposed on the basis of its complex eigenvectors $\mathbf{v}_n$ associated with real positive eigenvalues λ_n:

$$\mathbf{C}(f) = \sum_{n=1}^{N} \lambda_n(f)\mathbf{v}_n(f)\mathbf{v}_n^{\dagger}(f). \qquad (2)$$

Then eigenvalues are arranged in decreasing order and the covariance matrix spectral width is computed as a function of frequency as per Seydoux et al. (2016a):

$$\sigma(f) = \frac{\sum_{i=1}^{N}(i-1)\lambda_i(f)}{\sum_{i=1}^{N}\lambda_i(f)}. \qquad (3)$$

This spectral width metric corresponds to the width of the covariance matrix eigenvalues distribution and allows a compact time-frequency representation of the wavefield as it is recorded by the ensemble of stations composing the network. A low spectral width value indicates a tight eigenvalues distribution, meaning that the wavefield is dominated by one localized source generating coherent waves. On the contrary, a large spectral with value reflects a wavefield composed by multiple well-distributed sources generating incoherent waves. Therefore, the resulting spectral width value can be seen as a proxy of the number of independent sources composing the wavefield. It is thus effective in identifying temporal windows containing seismic energy emitted by a spatially well-located source (e.g. tremor), contrasting from windows dominated by distributed ambient seismic noise.

The parameter settings for calculating the covariance matrix depend on the signal of interest. However, as a general rule, the number of overlapping subwindows M should be at least equal to the number of stations of the network, to ensure statistically robust estimation of the covariance matrix. In addition, the duration of this sub-window δt, must be long enough to allow the wave to propagate through the entire network. So, with its 20 stations and aperture of around 15 km, the configuration of the PdF seismic network requires the large averaging time windows Δt to be at least a few minutes. This enables us to achieve satisfactory temporal resolution for the study of seismic tremor. However, for the study of co-eruptive impulsive earthquakes, we need a higher temporal resolution, and we therefore decide to apply a template matching method. It is indeed important to apply complementary detection methods together for a broader illumination of the different mechanisms at play during eruptions producing the large range of seismic signals recorded by the seismic network.

3.1.1.2. Locating seismic tremor using inter-station cross-correlations differential travel times. When a window containing seismic energy associated with a well-defined source is detected, the corresponding source can be located using the differential travel times contained in inter-station cross-correlations in order to "back-project" the signals energy toward its source via a grid-search approach (Ballmer et al., 2013; Droznin et al., 2015). The source location quality can be altered from scattering due to local heterogeneities and from imprecision of the velocity model described hereafter. In order to mitigate these effects, we apply a smoothing operation to derive the smooth envelope $S^{i,j}$ of the cross-correlations waveforms. To do so, we compute the absolute value of the analytic signal derived from the Hilbert transform, that we convolve with a Gaussian window using a 1.5 s width following Journeau et al. (2020). For every grid point $\mathbf{r} = x\mathbf{e}_x + y\mathbf{e}_y + z\mathbf{e}_z$, each inter-

station cross-correlation envelop $S^{i,j}$ is shifted by the time difference needed for the wave to travel from the tested source to the two stations i and j. We finally compute the function $R(\mathbf{r})$ by stacking at zero lag time the value of the shifted envelopes for all stations pairs as:

$$R(\mathbf{r}) = \sum_{i=1}^{N} \sum_{j=i+1}^{N} S^{i,j} \left[t^i(\mathbf{r}) - t^j(\mathbf{r}) \right] \tag{4}$$

with N the number of stations and $t^i(\mathbf{r})$ the travel time between the tested source and the station i. We compute those travel times using the Taup package of the ObsPy python toolbox (Beyreuther et al., 2010). The method for ray tracing and travel time computation is explained in Buland and Chapman (1983) and was originally implemented as the Taup toolkit by Crotwell et al. (1999). Topographic effects are considered by taking into account the seismic station elevations when computing the travel times. As we explore the full depth range extending from the volcano summit to 5.6 km below, we implement our 3D back-projection based on a body-wave assumption, considering that the tremor wavefield is dominated by shear waves. Therefore, we use a 1D S-wave velocity model of PdF derived by Mordret et al. (2015), represented in Fig. S1. This function $R(\mathbf{r})$ can be interpreted as a spatial likelihood function that defines the most probable location of a seismic source in a particular position of our 3D grid having a $100\ m$ x $100\ m$ x $100\ m$ spatial resolution.

This tremor location workflow was systematically applied to all co-eruptive periods as illustrated in Fig. S2. Setting the covariance matrix computation parameters to $M = 20$ and $\delta t = 20s$, we obtain its estimation over 200 s-long overlapping windows. We then filter the covariance matrix by its 1st eigenvector as suggested by Soubestre et al. (2019) before applying the back-projection grid-search approach. This filtering removes the noise spanned by higher-order eigenvectors and thus to focus on the dominant tremor source. We then retrieve the filtered inter-station cross-correlations in the time domain and stack them for five consecutive windows. We back-project the envelopes of those filtered cross-correlations in our 3D grid-search using the 1D S-wave velocity model described above. Finally, we extract the 3D tremor coordinates maximizing the resulting spatial likelihood function computed in 10 min-long time windows.

Assessing the accuracy of our inter-station cross-correlation location method can be done in two ways. It is first possible to measure the distance between the hypocenter of an earthquake estimated using the P and S wave arrival times, and the coordinates of the maximum of the spatial likelihood function computed for a time window containing this earthquake. While the resulting average misfit is about 7 km using DLP earthquakes located around 30 km below the Klyuchevskoy volcano (Journeau et al., 2022), the misfit is about 2 km or less using shallower VT hypocenters below the Izu-Oshima volcano (Permana et al., 2019). Then, we can also measure the spatial distribution oh the highest values of the tremor spatial likelihood function above a certain threshold, that we fix here to 98%. Journeau et al. (2022) shows an increase of the average vertical 98% error from 2 to 3 km for shallow tremor sources to about 10 km toward 30 km depth. We measured this vertical error for the first 10-min window of each PdF eruptions analyzed in this study, and we obtained an averaged error of 0.6 km. We illustrate this in Fig. S3 showing examples of the 98% contour values of the spatial likelihood functions for four different eruptions.

We note that the accuracy of our location method based on the back-projection of inter-station cross-correlations is sufficient for the study of seismic tremor. However, we need better spatial resolution for the study of co-eruptive impulsive earthquakes. We therefore decided to apply a double-difference algorithm to precisely re-locate earthquakes detected by template matching.

3.1.1.3. Classifying seismic tremor combining spectral width and network response function metrics. The network response function (NRF) is another covariance matrix metric designed to evaluate the level of focusing of the spatial likelihood function. We first normalize $R(\mathbf{r})$ by its sum over all grid points:

$$\overline{R}(\mathbf{r}) = \frac{R(\mathbf{r})}{\sum_{\mathbf{r}} R(\mathbf{r})} \tag{5}$$

and then add a temporal normalization by the maximum over the total time period:

$$\widetilde{R}(\mathbf{r}) = \frac{\overline{R}(\mathbf{r})}{max_t(\overline{R}(\mathbf{r}))}. \tag{6}$$

We defined $NRF(t)$ as the maximum of $\widetilde{R}(\mathbf{r})$, which is expected to be high for well localized sources and low for a random incoherent wavefield.

The comparison of the resulting NRF with $\overline{\sigma}$, the spectral width function averaged in a given frequency band ([0.5–5] Hz), defines a plane where all the detected signals can be classified between continuous tremor-like signals and impulsive earthquake-like signals thanks to their contrasting wavefield characteristics measured by the seismic network (Journeau et al., 2020, 2022). We show the resulting wavefield classification for the 2014–2021 period at PdF in Fig. S4.

Note that the red lines in Fig. S4 are manually defined to visually separate the different detection groups observed in the 2D NRF-SW space. We consider a temporal window as a detection if $\overline{\sigma} < 0.78$ and $NRF > 0.2$. Then, we defined the oblique red line following this equation: $SW_{tremor} = -0.6 \times NRF + 0.9$, and a detection is classified as tremor if $\overline{\sigma} < SW_{tremor}$, or as earthquake if $\overline{\sigma} > SW_{tremor}$. Tremor-earthquake detections follow such a distribution in this NRF-SW plane because, compared to earthquake, tremor sources emit more energy in the [0.5–5] Hz frequency band where $\overline{\sigma}$ had been averaged (leading to lower $\overline{\sigma}$ values for tremor), and tremor wavefield back-projection is less well-focused (leading to lower NRF values for tremor). In order to provide an automatic wavefield classification scheme effective for monitoring purposes, future work would be required taking advantage of machine learning methods.

3.1.1.4. Seismic tremor characterization from its time-frequencies properties and cross-spectra phases. As shown in Soubestre et al. (2021), the detailed analysis of the spectral width function corresponding to a detected tremor source enables to follow the time-frequency properties of the associated tremor signal.

Moreover, it has been shown that the inter-station cross-correlation waveform is very sensitive to modifications of the tremor source mechanism or change of its position and can be used as a "fingerprint" of the tremor source (Droznin et al., 2015). Therefore, this information encoded in the phase of the cross-correlation waveforms is complementary to the spectral content information obtained from the eigenvalue-based analysis described above. Droznin et al. (2015) computed a Pearson correlation coefficient between different consecutive windows of single-pair cross-correlation as a measure of their waveform similarity. Soubestre et al. (2018) extended this approach to the whole network using the first eigenvector of the covariance matrix as a fingerprint. These vectors being complex, they defined the correlation coefficient at each frequency as the absolute value of the complex scalar product normalized by the respective norms. They finally obtained a 2D time-time matrix containing all the correlation coefficients values by computing an average correlation coefficient in a given frequency band ([0.5–5] Hz in our case).

We apply this method for the December 2020 PdF eruption, using same parameterization as the one used for the spectral width computation ($M = 20$, $\delta t = 60s$) in order to compare the results from these two methods and to characterize the seismic tremor and its evolution during the eruption.

3.1.2. Template-matching for detecting the discrete "gas-pistons" signals

We have developed a new approach to detect the transition between continuous tremor and intermittent tremor composed of individual gas-pistons appearing during the final phases of eruptions. Namely, we use an automatic single station three-component template-matching method for gas-pistons detection and counting. It is based on the fact that each of these observed seismic events (lasting approximately 10-s) are very similar between each other and, therefore, behave as multiplets.

Selecting a 15-s template and performing a classical template-matching method scanning the continuous data, we can detect additional gas-piston events in the sequence. However, we also observe in some cases that frequency content of these gas-piston events evolves with time. Therefore we adjusted the basic template-matching procedure in order to not have to manually select a single template.

As a first step, we select the closest seismic station to the active eruptive vent to enhance signal-to-noise ratio. We then cut 1-day data stream into 30-min-long time windows, each of them being sub-divided into 15 s long segments overlapping at 10% of their size, obtaining $N = 11,901$ subwindows. We compute correlation coefficient between all 15-s subwindows of the large 30 min window and therefore end up with a 2D matrix (NxN) containing the correlation coefficient values. These operations are done for the 3 components of the selected seismic station and we stack the resulting correlation coefficient matrices.

Fixing a threshold for a correlation coefficient value of 0.4, for each 15-s subwindow, we can count the number of similar 15-s events occurring within the long 30-min window and thus obtain a 1D function quantifying the number of similar events in the 30-min window. Fig. S5 summarizes all of these operations.

Finally, we smooth in time the 1D function and we only count the number of maxima of this function to obtain a proxy of the number of individual gas-piston events in a given time window. We systematically apply this method over the 2014–2021 time period to better constrain the transition from continuous tremor toward the gas-piston phenomenon.

In addition to the tremor properties mentioned above, we also track the seismic tremor amplitude using the RSAM (raw seismic amplitude measurement) (Endo and Murray, 1991).

3.1.3. Detection and relocation of co-eruptive earthquakes

We also track the co-eruptive impulsive seismic signals that can be of different types and generated in different locations of the shallow system. We detect these earthquakes with a template matching approach following the same approach as Lengliné et al. (2016) and Duputel et al. (2019). We use 25 templates signals of 5.12 s starting 1 s before the P-wave arrival with a large signal/noise ratio during the considered period. Seismic waveforms and spectra of these templates are shown in Fig. S6. Template matching is conducted using three 3-component stations in the vicinity of the eruptive site (FOR, VIL and CSS, see Fig. 1 for location). The detection threshold is set from a fixed probability of false detection of 10^{-5} per year per template, following Lengliné et al. (2021). We show four seismic waveforms examples of newly detected earthquakes in Fig. S7. The detected earthquakes are then re-located using a double-difference relative location algorithm (Waldhauser and Ellsworth, 2000).

We thus detect and re-locate co-eruptive earthquakes during the July–August 2017 eruption as an example.

3.2. Estimation of lava discharge rate from satellite data

Once the effusive phase of an eruption has started, the quantitative evaluation of the lava flow at the eruptive event, which we will refer to as TADR (Time averaged Discharge Rate), becomes available. Knowledge of the lava flux time evolution throughout an eruption is important to better understand its shallow dynamics, and better interpret the corresponding tremor observations.

For our study, we considered TADR data measured from thermal data

acquired by two systems: MIROVA (Coppola et al., 2009, 2020) and HOTVOLC (Gouhier et al., 2016). The MIROVA system (Middle Infrared Observation of Volcanic Activity) - an automatic volcano hot spot detection system based on the analysis of MODIS data (Moderate Resolution Imaging Spectroradiometer) - provides approximately 2–4 images daily at a resolution of 1 km. HOTVOLC - a web-based satellite-data-driven monitoring system using data from the geostationary satellite Meteosat - provides images with higher sampling rate (around 15 min) but with less precision.

We selected ten eruptions (May 2015, August–October 2015, September 2016, January–February 2017, July–August 2017, April–June 2018, September 2018, February–March 2019, April–May 2021 and December 2021–January 2022) for which robust TADR measurements are available. We then use these 10 eruptions as a sub-database for which we also look at geodetic and petrologic data in addition to the seismic data previously introduced.

3.3. Volcanic edifice deformation from GNSS baselines measurement

We track the time evolution of the volcanic edifice deformation by computing the baselines, i.e., the distances between summit stations DSRG and SNEG (see location on Fig. 1). The increase or decrease of these baselines over time can highlight the inflation or deflation of the volcanic edifice, potentially linked to a replenishment of the shallow magmatic reservoir or its emptying, respectively. Thus, the monitoring of these baselines allows us to have a simple proxy of the state of the shallow system during the eruption. Daily GNSS solutions have been computed by OVPF-IPGP with the GipsyX precise point positioning (PPP) software (Bertiger et al., 2020).

3.4. Insights into PdF dynamics from lava products analysis

We then compare the information drawn from the previously introduced geophysical data with that obtained from the analysis of the lava. This allows us to have a more complete vision of the eruptive dynamics at the PdF, such as the H_2O degassing depth and the original depth of erupted magma (shallow reservoir or deeper).

3.4.1. Gas volume fraction estimation from inclusions

We use the Eq. 7 defined in Villemant and Boudon (1998) to obtain an estimate of the percentage of gas volume fraction (χ) in the melt as a function of the depth during its ascent, reflecting the amount of exsolved gas bubbles.

$$\chi(\%) = \frac{K_R \times \Delta X_{H_2O}}{P}, \tag{7}$$

where $\Delta X H_2O = X_{H_2O}(P_0, T_0) - X_{H_2O}(P, T)$, with $X_{H_2O}(P, T)$ the dissolved H_2O content in magma at pressure P and temperature T, and $X_{H_2O}(P_0, T_0)$ the initial water content at the shallow magma reservoir level, setting $T_0 = 1100°C$ and $P_0 = 49 MPa$ corresponding to a depth of 2000 m below the surface (using $P_0 = \rho_s g z$, with $\rho_s = 2500 kg/m^3$ the medium density and $g = 9.81 m/s^2$ the gravity acceleration). We set the constant value $K_R = 15$, corresponding to a magma temperature $T = 1100°C$ and a magma density $\rho_s = 2500 kg/m^3$.

Given that CO_2 has already more or less completely degassed at this depth, the dominant gaseous species in the shallow system is H_2O (Sparks (2003); Di Muro et al., 2016). We therefore only consider the degassing of dissolved H2O as a contribution of bubble fraction in rising magma.

The amount of dissolved H_2O in the PdF magma is inferred from the analysis of primary melt inclusions hosted in olivines (Di Muro et al. (2016)) using the Eq. 8 fitting a population of 130 MIs (Melt Inclusions) analyses:

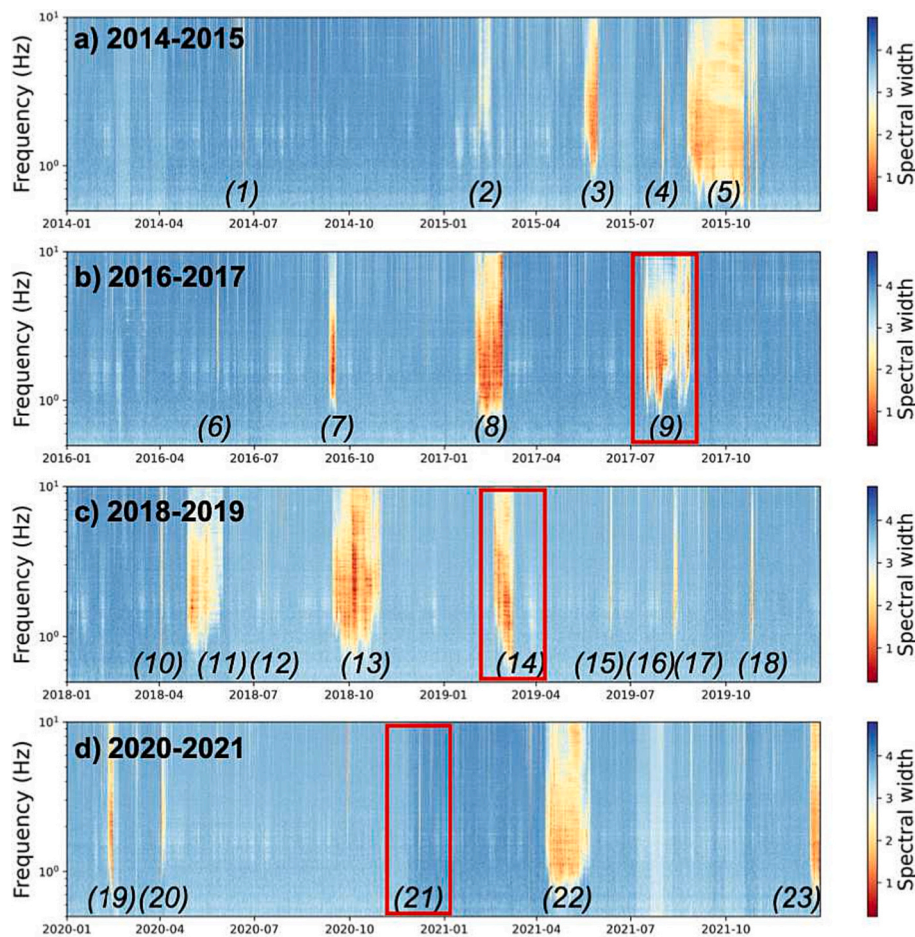$$X_{H_2O}(P, T)(wt\%) = C1 \times log(P) + C2 \times e^{C3 \times T} + C4 \tag{8}$$

Fig. 2. Co-eruptive tremor seen as high spatial coherence seismic signals. Seismic network covariance matrix spectral width computed for the a) 2014–2015, b) 2016–2017, c) 2018–2019, d) 2020–2021 time periods. The numbers from 1 to 23 correspond to the 23 eruptions that took place in this time period. Red rectangles highlight three selected eruptions for which we show zoom of their spectral width in Fig. 4 (December 2020), Fig. 6 (July–August 2017) and Fig. 11 (February–March 2019). (For interpretation of the references to colour in this figure legend, the reader is referred to the web version of this article.)

where $C1 = 0.1759$, $C2 = 4.019e - 31$, $C3 = 0.0556$, $C4 = 0.164$ are constants and $T = 1100°C$ is the magma temperature that we consider constant, assuming that the magma does not cool down significantly during its ascent toward the eruptive site.

3.4.2. Magma chemical composition estimation from petrologic data

A final piece of information that we wish to compare with the seismic observations is the chemical composition of the eruptive products from analysis of major element compositions in bulk rocks (Coppola et al., 2017; Gurioli et al., 2018; Vlastélic et al., 2018; Thivet et al., 2020a, 2020b). We focus in particular on evolution of MgO ($wt\%$) content of these inclusions, which is proportional to melt temperature and crystal accumulation, and CaO/Al_2O_3 ratio, which is proportional to melt temperature and evolution (Di Muro et al., 2016). At PdF, the phases of high lava output rate are usually associated with both hotter melts and a higher content of crystals (Coppola et al., 2017).

4. Results

4.1. Co-eruptive seismic tremor catalog

First, we systematically applied the covariance matrix method described in the previous section to the continuous seismic data of the PdF network throughout the 2014–2021 time period. We show the resulting 8-years time series of covariance matrix spectral width in Fig. 2, highlighting the seismic signature of the 23 eruptions (see

Table 1) and to characterize their spectral properties.

Tremor can be separated from other seismic signals computing the NRF and comparing it to the 1D averaged spectral width function (as explained in section 3). We show in Fig. S4 the resulting distribution of all analyzed temporal windows in the NRF versus spectral width plane. Windows located in the "noise" area are characterized by a low spatial coherence level with respect to the "tremor" and "earthquakes" areas for which corresponding windows are defined such as "detection".

We show in Fig. 3a the temporal evolution of the daily percentage of detection. Starting with 860,860 10-min-long overlapping windows, we obtain 103,446 tremor detections and 41,415 earthquake detections. Our analyzed time period span 23 eruptions corresponding to a total of 358.7 days of eruptions. In comparison, our automatic method detects in total 345.8 days of tremor during co-eruptive periods, or 96.4% of the cumulative eruptive time in our considered time period. The eruptive periods without tremor detection (about 12 days in total) might be linked to phases of low level of volcanic activity with weak surface manifestations due to low amount of gas in the conduits. Indeed, such configuration might in turn generate a tremor source too weak to exhibit strong coherence across the 15-km network, which consequently falls below the detection threshold defined by our metrics derived from the network covariance matrix.

In contrast, 4.3% of our total number of tremor detection occur during inter-eruptive periods. These windows classified as tremor outside eruptions may be associated with periods of high swell, cyclone passage, or volcanic tremor-like signals previously unidentified. More

Table 1

List of the 23 eruptions that occurred in the 2014–2021 time period (and December 2009 eruption) and specification of their characteristics. *Note that the terminal phases of the eruption of August–October 2015 are not associated with gas-piston. The gas-pistons are observed only between the phases of renewed eruptive activity (see Fig. S16).

Eruption timing (dd.mm.yyyy hh:MM)	Duration (days)	Distance from summit (m)	Gas-piston
14.12.2009 14:40–15.12.2009 06:30	0.7	525	yes
20.06.2014 21:35–21.06.2014 17:09	0.8	570	yes
04.02.2015 06:50–15.02.2015 18:30	11.5	770	yes
17.05.2015 09:45–30.05.2015 16:50	13.3	1100	yes
31.07.2015 05:20–02.08.2015 07:15	2.1	2000	yes
24.08.2015 14:50–31.10.2015 04:02	58.3	1135	no*
26.05.2016 04:05–27.05.2016 07:40	1.1	2900	yes
11.09.2016 04:41–18.09.2016 00:18	6.8	1425	no
31.01.2017 15:40–27.02.2017 15:30	27.0	2000	yes
13.07.2017 20:50–27.08.2017 23:00	45.1	1700	yes
03.04.2018 06:40–04.04.2018 00:00	0.7	3450	yes
27.04.2018 19:50–01.06.2018 10:30	34.6	1550	yes
12.07.2018 23:30–13.07.2018 18:00	0.8	1680	yes
15.09.2018 00:25–01.11.2018 00:00	47.0	2010	yes
18.02.2019 05:48–10.03.2019 18:00	19.1	2500	no
11.06.2019 02:35–13.06.2019 08:00	2.2	500	yes
29.07.2019 08:00–30.07.2019 00:30	0.7	2250	yes
11.08.2019 12:20–15.08.2019 00:20	4.1	3500	yes
25.10.2019 10:40–27.10.2019 12:30	2.1	6250	yes
10.02.2020 06:50–16.02.2020 10:12	6.1	600	yes
02.04.2020 08:20–08.04.2020 09:30	4.2	1940	no
07.12.2020 00:40–08.12.2020 03:15	1.1	1700	yes
09.04.2021 15:00–23.05.2021 22:00	44.3	2771	yes
21.12.2021 23:30–16.01.2022 22:10	26	1700	no

detailed and specific studies of these windows will be required in the future.

Fig. 3b and c show the epicenters and depths of the located co-eruptive tremor sources, respectively. We observe that co-eruptive tremor sources are systematically located close to eruptive sites and mainly concentrated a few hundreds of meters beneath the surface (98% of tremor sources are located between 200 m depth and the surface). This shallow level beneath eruptive sites correspond approximately to the depth range where gas exsolution accelerates strongly going from about 1% to more than 20% of gas volume fraction in a few hundred of meters. Such correlation between the depth profile of gas volume fraction and number of tremor source suggests that the mechanism of tremor generation is strongly controlled by the shallow magma degassing when it approaches the surface and the eruptive vent.

4.2. Time-frequency properties of co-eruptive seismic tremor

We selected as examples two eruptions whose details are presented in this section. We focus on the covariance matrix spectral width time evolution of a short-lived eruption (December 2020) and a long-lived eruption (July–August 2017). We show how tracking their time-frequency properties help to infer changes in the underlying degassing regimes. We can therefore compare the resulting eruptive dynamics evolution for those two different scenario. While the short-lived December 2020 eruption involves simpler eruptive phases transitions, the July–August 2017 one is more complex. For this latter, we compare its tremor properties variations with other observations presented previously. We finally describe the February–March 2019 eruption to illustrate an example of an end-of-eruption characterized by an effusive paroxysm contrasting with the more usual gas pistons events.

4.2.1. Short duration December 2020 eruption

The December 2020 eruption lasted approximately one day between 07.12.2020 (00:40) and 08.12.2020 (03:15). We show in Fig. 4a-c the time evolution of the co-eruptive tremor spectral content, amplitude, state (when detected seismic gas-pistons swarm marks transition from continuous to intermittent tremor) and temporal stability (via first eigenvector similarity). We can thus observe the non-stationarity of volcanic tremor during the eruption evolving through different phases.

Two photos of the eruptive site are shown in Figs. 4d,f, taken in two distinct eruption phases (initial phase (1) and intermediate phase (2)) with contrasting seismic tremor properties (Fig. 4a-c). The image shown in Fig. 4d illustrates the Hawaiian lava fountain activity all along the opened eruptive fissure, as it is usually observed during initial phases at PdF. The onset of this phase was characterized by a large activated frequency band, in particular with low frequencies excited below 1 Hz, associated with a high tremor amplitude. Those lowest frequencies gradually ceased to be excited, simultaneously with a tremor amplitude decrease.

A stabilization of tremor properties marked a transition in eruption phases. Fig. 4f at the end of this transition phase, reveals that the eruptive activity has focused on a single vent. At that time, we observe a Strombolian eruptive activity when the activated tremor frequency band starts to widen (without the initial low frequencies), with small tremor amplitude fluctuations and new phase of tremor stability (Fig. 4a-c).

The tremor state can be considered as continuous during the initial phase (1) and the beginning of the intermediate phase (2). However, at the end of the second phase, we start to detect some discrete seismic gas-piston events within the tremor. This marks a transition toward the final phase (3) in which tremor spectral content evolves toward higher frequencies and tremor amplitude decreases until reaching the background noise level. In this last phase, no more lava effusive activity was observed at the surface, only intermittent degassing occurred (as illustrated in Fig. 4f for another eruption), probably linked with each tremor burst detected as gas-piston events.

The different magma degassing regimes associated with the eruption phases (1), (2), (3) and with changes in tremor characteristics are schematized in Fig. 5a, using illustrations from Spina et al. (2019) and typical gas volume fraction values from Vergniolle and Gaudemer (2015). Note that these gas volume fraction values are only indicative and do not take into account the potential accumulation of pre-eruptive bubbles in the shallow reservoir, nor the significant expansion of bubbles very close to the surface.

It is known from several volcano geodesy studies that deformation induced by magma transport through dykes can be modeled by rectangular tensile cracks (Okada, 1985). We therefore decided to consider the shallow dyke portion beneath eruptive sites as such and to interpret our observations of tremor spectra fluctuations during the initial and final
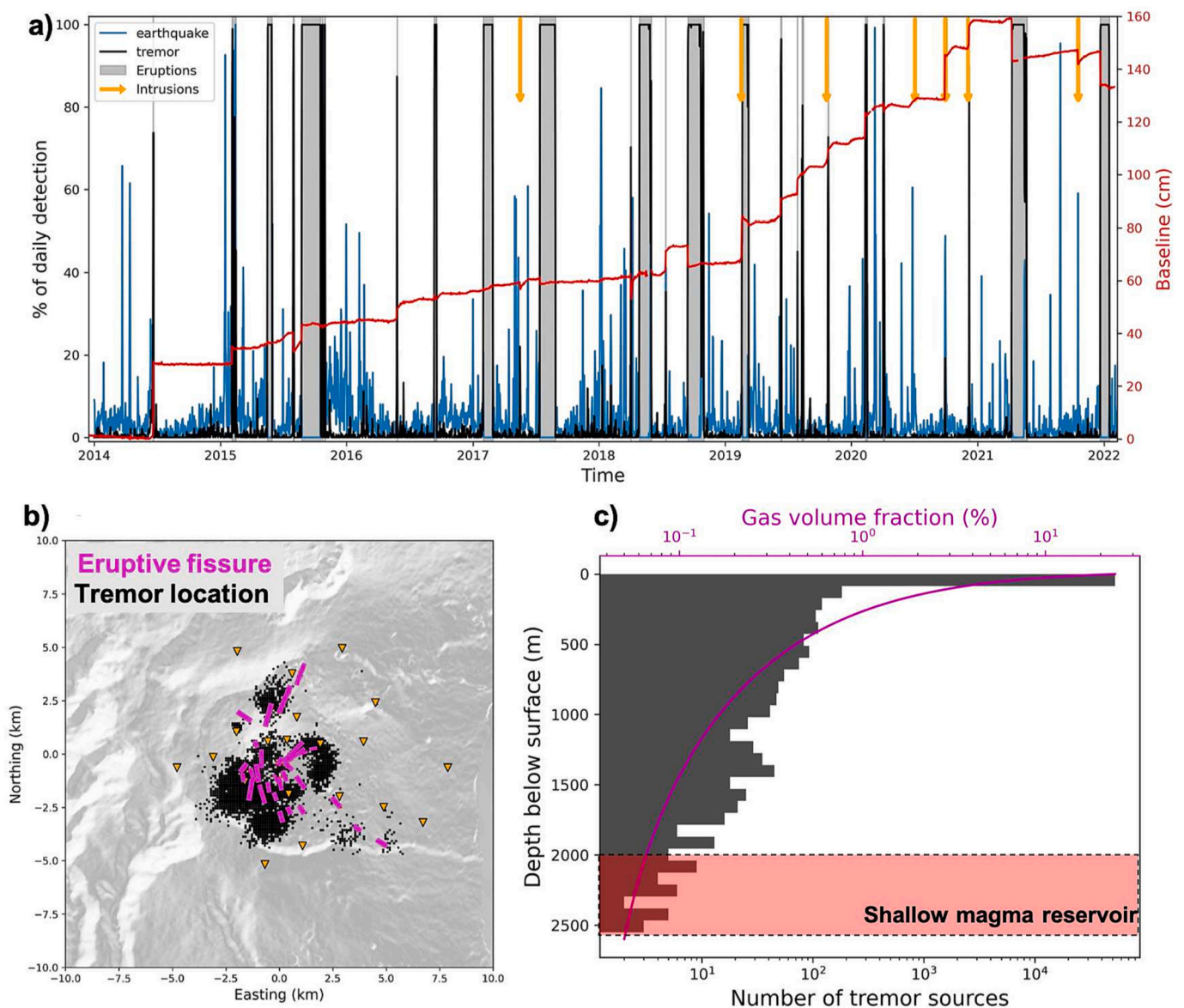
Fig. 3. Shallow co-eruptive tremor marks strong magma degassing beneath eruptive sites. a) Temporal evolution of daily detection percentage of tremor (in black) and earthquake (in blue) signals. Grey rectangles highlight the eruptive time periods while vertical downward orange arrows stand for intrusions (i.e. magma injection that did not reach the surface). The red curve represents for the DSRG-SNEG GNSS stations baseline time series. b) Tremor sources locations corresponding to the 23 eruptions that occurred in the January 2014–February 2022 time period. Black dots stand for the tremor source position and magenta lines for the eruptive fissures. Orange triangles indicate the seismic stations used during the cross-correlation back-projection procedure allowing tremor source location. c) Histogram of tremor source depths (logarithmic scale). The magenta curve indicates the modeled amount of exsolved gas from the magma as a function of depth during the magma ascent from the shallow reservoir, whose depth is indicated with a red rectangle. (For interpretation of the references to colour in this figure legend, the reader is referred to the web version of this article.)

phases using a resonant fluid-filled crack model (Chouet, 1996; Maeda and Kumagai, 2017) schematized in Fig. 5b. Corresponding equations from Maeda and Kumagai (2017) are detailed in the supplementary file.

The resonance frequency is mainly controlled by the crack geometry and the properties of its filling magma, in particular its bulk modulus and sound velocity associated with the gas volume fraction. The observed tremor frequency increase in phases (1) and (3) can be linked to either a decrease in the dyke dimension (associated with the focus of the eruptive activity on a single vent, dyke closing, and/or decrease in resonating lava column length) or a decrease in conduit gas content (explaining changes in the observed varying degassing regimes).

4.2.2. Long-duration and complex July–August 2017 eruption

We represent in Fig. 6 the temporal evolution of a set of 5 parameters characterizing the dynamics of the 47-days-long July–August 2017 eruption. In addition to seismic tremor properties (Figs. 6a-b) that we present in the previous section for the short December 2020 eruption, we also track in time the lava discharge rate at the eruptive vent (Fig. 6c) as well as the volcanic edifice deformation and co-eruptive impulsive seismicity (Fig. 6d). This multi-disciplinary dataset enables to gain further insights into the functioning of long-lived and more complex eruptions.

4.2.2.1. Eruptive initial phase and focus of the activity at a single vent.

Figs. 7b-d represent a zoom of the initial phase of the July–August 2017 eruption lasting slightly more than one day, which is characterized by gradual loss of low tremor frequencies excitation, and simultaneous decrease of tremor amplitude and lava discharge rate.
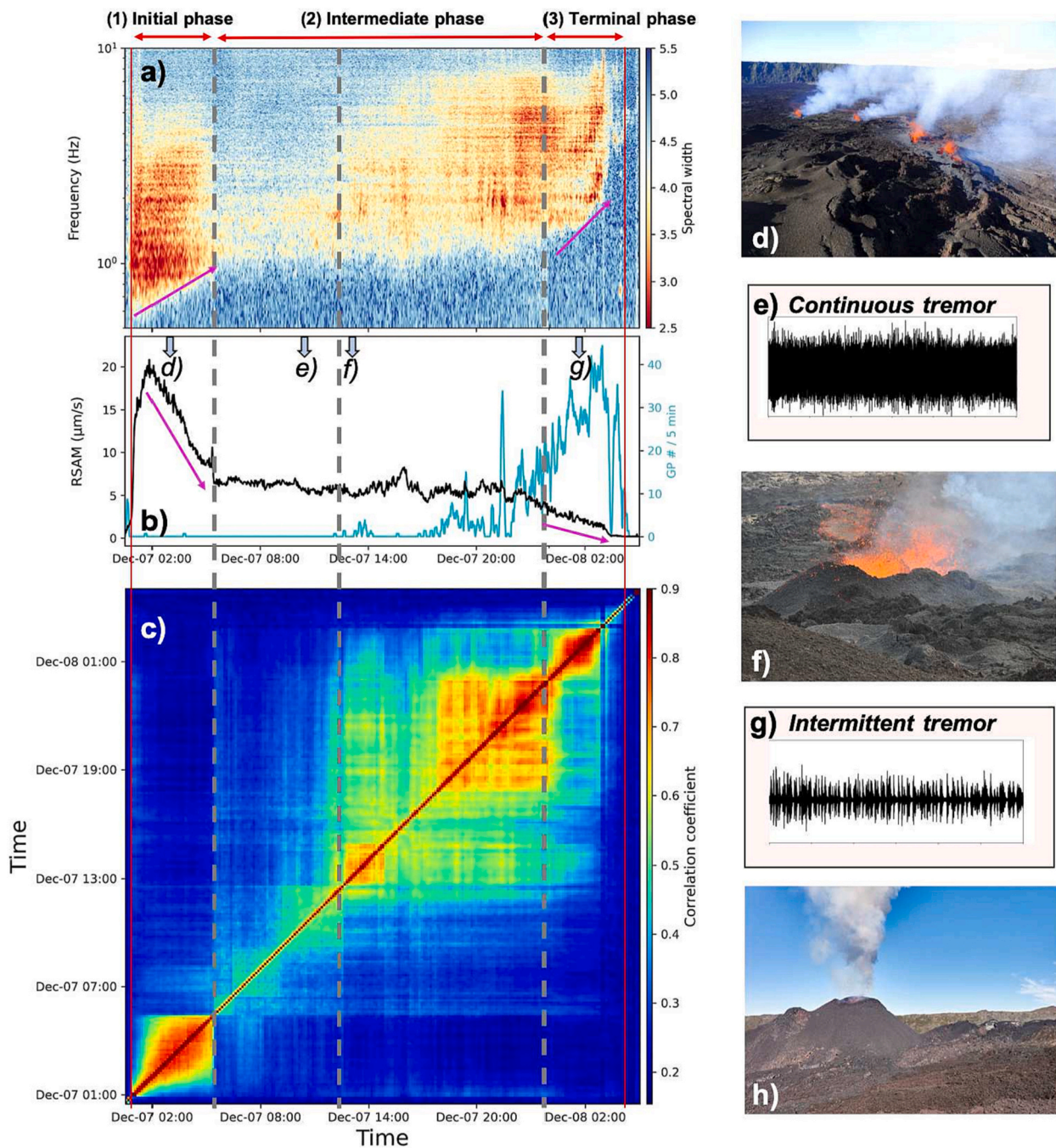
Fig. 4. Shallow liquid-gas dynamic controls time-frequency co-eruptive tremor properties, example from the short-time December 2020 eruption. a) Covariance matrix spectral width computed for 07.12.2020 and 08.12.2020. b) Black line represents tremor RSAM computed for the vertical component of the BOR station. Cyan line shows the result of the procedure of detection and counting of multiplets (seismic gas-piston events) in a final window of 5 min using BOR as a reference station. c) Matrix of correlation coefficients between covariance matrix's first eigenvector obtained by averaging all matrices computed in the [0.5–5] Hz frequency band. Vertical red lines in a), b) and c) indicate the beginning and the end of the eruption. The grey dashed lines indicate notable changes in tremor properties associated with changes of the temporal stability of the tremor interpreted as degassing regime transitions. Three identified phases ((1) initial, (2) intermediate and (3) final are reported on top of a). Purple arrows in a) and b) highlight simultaneous increase in tremor spectral content and decrease in tremor amplitude, during the initial and final phases. d) Photo showing the opening of the eruptive fissure over approximately 500 m with lava fountains. e) and g) are one hour seismograms recorded on the vertical component of BOR station, showing continuous and intermittent (composed of gas-pistons) seismic tremor in the initial and final phase of the eruption, respectively. f) Photo testifying the focus of the eruptive activity on a single vent with construction of a small eruptive cone and gradual transition toward a Strombolian degassing regime. Timing of photos d) and f) and seismograms zoom e) and g) are indicating in b) with light blue vertical downward arrows. h) Photo of a well-developed eruptive cone during a gas-piston degassing phase without lava effusion. It was taken during another eruption in October 2018 and we show it because such a photo was not available for the December 2020 eruption. (For interpretation of the references to colour in this figure legend, the reader is referred to the web version of this article.)
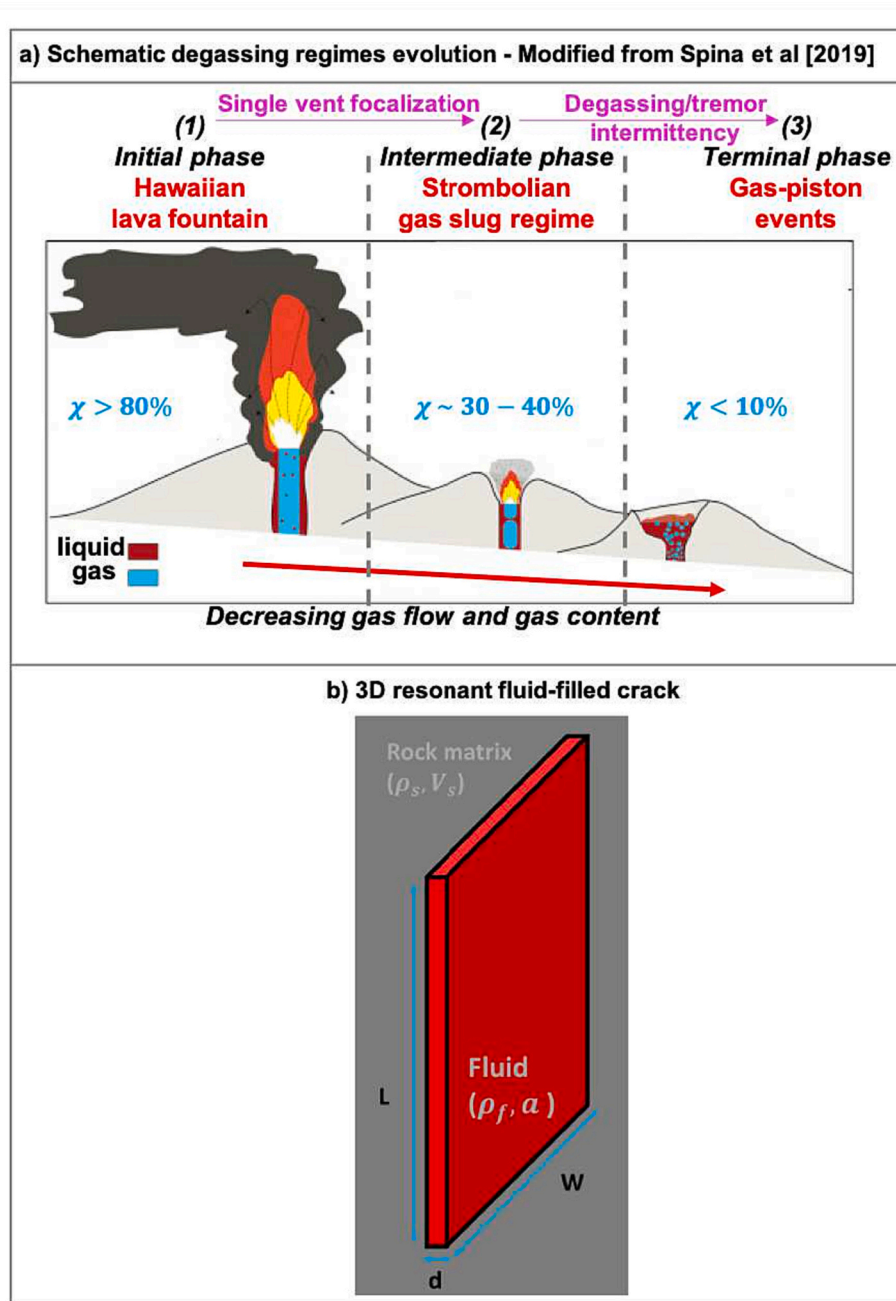
Fig. 5. Schematic representation of different phases of magma degassing regimes and tremor spectra fluctuations interpretative framework. a) Figure modified from Spina et al. (2019) showing evolution of degassing regimes while gas flow and gas content decrease over time. b) Schematic 3D fluid-filled crack with main parameters, namely crack geometry and magma properties, controlling the crack resonance frequencies.

As it was the case for the short December 2020 eruption, the images of the eruptive site shown in Fig. 8a illustrate distributed Hawaiian lava fountains activity during the initial phase while the activity has focused on a single vent at the end of this first phase, with the start of an eruptive cone edification resulting from the accumulation of volcanic products.

We report in Fig. 7e the initial minimum excited tremor frequency as a function of the length of the eruptive fissure opened at the surface for the 23 eruptions of our catalog. From this distribution, a decrease of the tremor frequency with an increase of the fissure length is observed, suggesting that initial tremor spectra are controlled by a characteristic size over which shallow degassing occurs, that might reflect the width of the dyke head arriving at the shallow gas exsolution level. Then, the gradual increase of tremor frequency content during initial phases can be linked to the progressive focus of the activity on the eruptive fissure.

Selecting seven eruptions for which TADR data are available during their initial phases (Fig. S8a), we show in Figs. S8b,c the relationships between tremor minimum excited frequency, tremor amplitude and the lava discharge rate, revealing a systematic tremor frequency increase concomitant with tremor RSAM and TADR decrease over time. We therefore suggest that observations reported in Figs. 7b-d can be generalized to others PdF eruptions in their initial phases.

4.2.2.2. Eruptive intermediate phase: cone instabilities and magma re-feeding. Intermediate phases of PdF eruptions are more complex for long-lived rather than short-lived eruptions. This phase lasted 37 days for the July–August 2017 eruption and was characterized by strong fluctuations in tremor spectra and amplitude (Figs. 6a,b) based on which
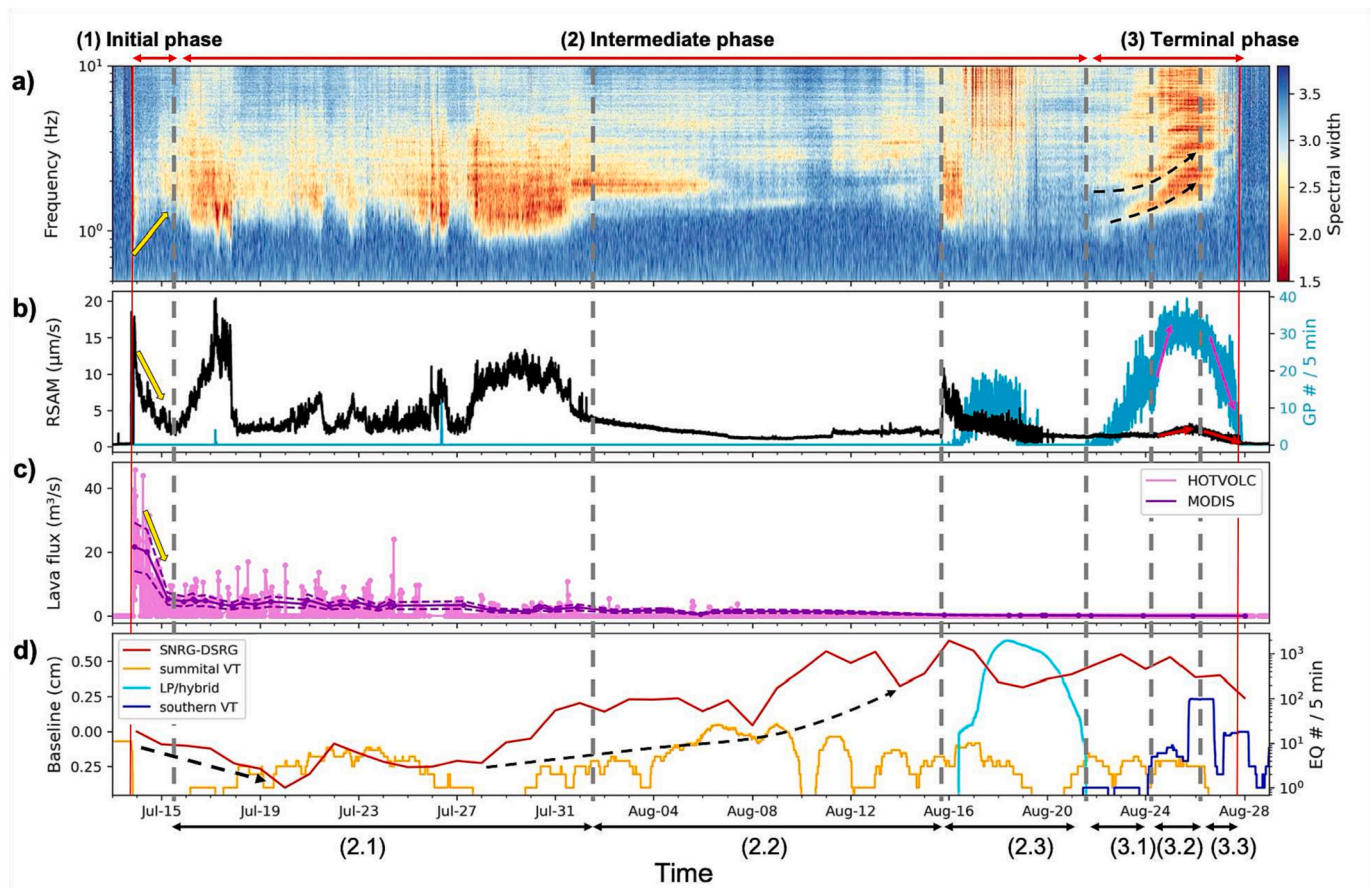
Fig. 6. Co-eruptive tremor fluctuations during the long-lived July–August 2017 eruption. a) Covariance matrix spectral width as a function of time and frequency computed in 2-min-long time windows. The two dashed black arrows highlight some spectral gliding during the final phase. b) Black curve represents the amplitude of the tremor estimated by calculating the RSAM on the FOR station (vertical component, filtered between 0.5 and 5 Hz). Cyan curve represents the number of detected gas-pistons in 5-min-long time windows. No gas piston events are detected during periods of continuous eruptive tremor. c) Lava discharge rate (TADR) data obtained by 2 different satellite platforms: MIROVA (purple line) and HOTVOLC (light purple line). Yellow arrows during the initial phase in a), b) and c) highlight the cessation of lowest tremor frequencies activation, and the decrease of RSAM and TADR, respectively. d) Red line shows summit deformation illustrated by the daily baseline between 2 summit GNSS stations (DSRG and SNEG, see location on Fig. 1). Orange, cyan and blue lines represent the number of detected and located summit VTs, LP/hybrids and southern VTs earthquakes, respectively. The dotted black arrows highlight a tendency of deflation of the edifice at the beginning of the eruption and inflation in the middle of the eruption. The two vertical red lines indicate the start and end of the eruption, while grey dashed vertical lines stand for notable changes in the eruptive dynamics. (For interpretation of the references to colour in this figure legend, the reader is referred to the web version of this article.)

we can cut this long phase in three sub-phases, namely (2.1), (2.2) and (2.3) indicated at the bottom of Fig. 6.

At the beginning of phase (2.1), we note an edifice deflation (Fig. 6d), which started with the eruption, suggesting the shallow magma reservoir was still being emptied to fed the dyke and the eruption in surface. During that time, lava flux at the focused eruptive vent had still significant values (Fig. 6c). Therefore the eruptive cone started to grow at the end of the initial phase (Fig. 7a), and grew up more rapidly during the increase in RSAM (Fig. 6a). We note that the end of the volcanic edifice deflation episode is marked by the occurrence of shallow VTs earthquakes above the shallow reservoir (Fig. 6d) whose location are shown in Fig. 9.

We show in Fig. S9 a zoom on phase (2.1) with photos of the eruptive cone exhibiting several periods of destabilization. We highlight periods of increased amplitude and low frequency activation in the tremor that appears to be associated with cone building/closing. During periods when the cone flank collapsed, the amplitude of the tremor returns to a lower level and the low frequencies are no longer excited. In this phase, the increases in RSAM are not correlated with TADR increase. However, tremor properties might be modulated by non-stationary magma refeeding. Such magma pulses in the dyke can result in eruptive cone growth and in the increase of resonating lava column length potentially

explaining the intermittent activation of low tremor frequencies associated with increases in tremor amplitude.

In phase (2.2), we observe a weakening in co-eruptive tremor intensity during approximately two weeks (Figs. 6a-b), while TADR values were very weak (Fig. 6c) and notable changes in the summit GNSS stations baseline occured (Fig. 6d). The corresponding inflation of the volcanic edifice can be interpreted as magmatic recharge of the shallow reservoir while the eruptive activity in surface was low. Shallow VTs earthquakes were located between the volcano summit and the shallow reservoir during that period (see Fig. 6d and Fig. 8).

At the end of this volcanic edifice inflation on 15.08.2017, phase (2.3) started with an abrupt tremor amplitude increase and reactivation of its low frequencies (at around 1 Hz). According to the OVPF's volcanological activity bulletin, weather conditions were too cloudy to allow reliable estimates of lava flux that day, but tremor changes could be associated with a resumption of ephemeral lava fountain activity at the eruptive site, observed by one of the observatory's cameras (http://volobsis.ipgp.fr/volcano-reports/2017/08/OVPF_20170816_01_eruption.pdf). Such increase of the eruptive activity in surface was probably associated with a new arrival of magma from the shallow reservoir. As seen in Fig. 6b, about one day after the start of phase (2.3), multiplets are detected in the continuous
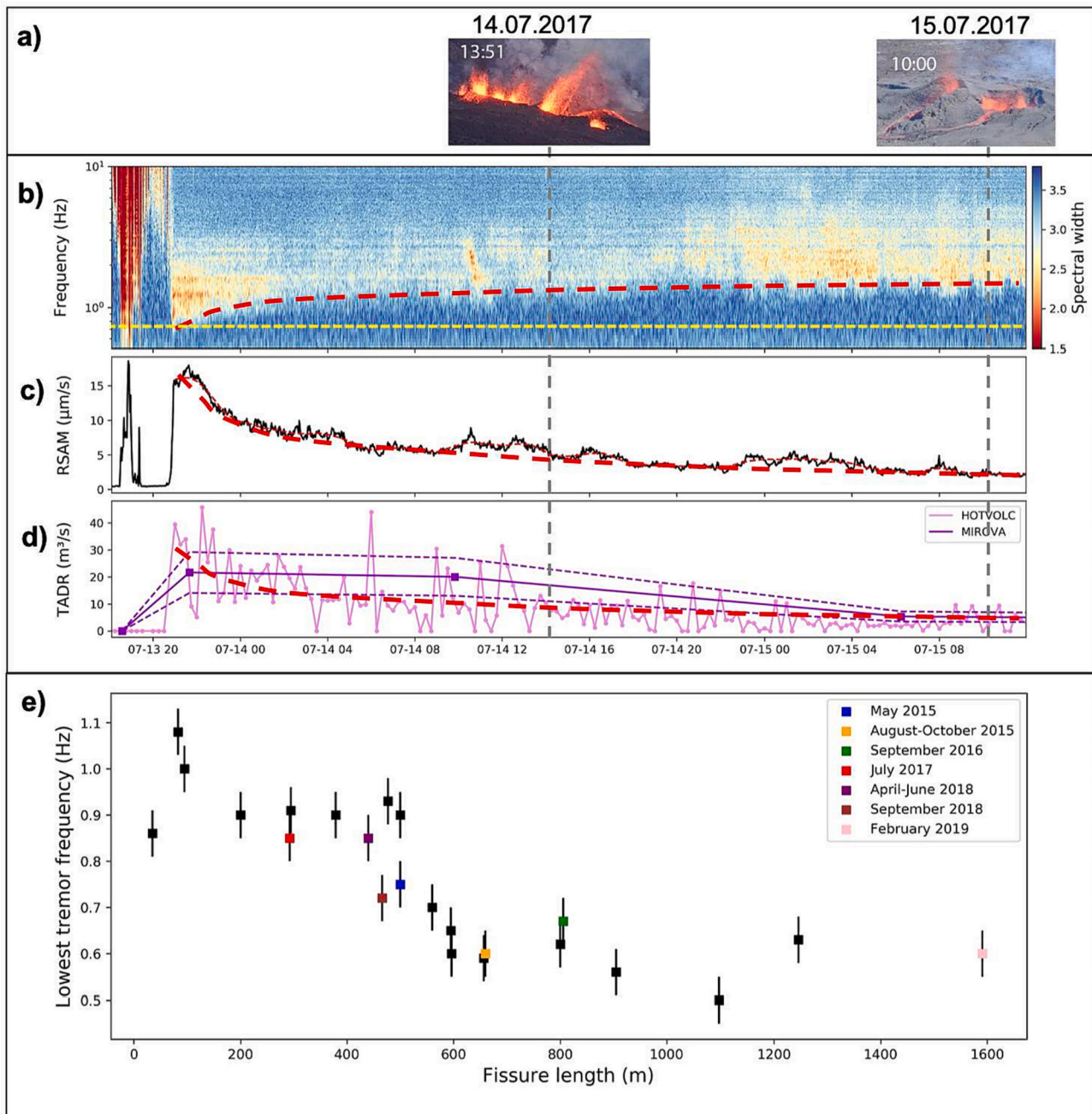
Fig. 7. Tracking seismic tremor changes while eruptive activity focus in a single vent during initial phase. a) Two photos of the eruptive site showing lava fountains on the initial fissure (14.07.2017–13:51) and the eruptive cone, which started to build about 20 h later (15.07.2017–10:00). These photos were taken during OVPF reconnaissance missions (© OVPF/IPGP). b) Covariance matrix spectral width as a function of time and frequency computed in 2-min-long time windows. The yellow horizontal dashed line indicates the minimum tremor frequency excited in the initial phase. c) Black curve represents the amplitude of the tremor estimated by calculating the RSAM on the FOR station (vertical component, filtered between 0.5 and 5 Hz). d) Lava discharge rate (TADR) data obtained by 2 different satellite platforms: MIROVA (purple line) and HOTVOLC (light purple line). The red curves in b), c) and d) represent interpretative trends following the gradual cessation of low frequencies excitation and the decreases in tremor amplitude and lava discharge rate. e) Minimum tremor frequency excited in the initial phase as a function of the total initial opened fissure length reported for the 23 eruptions of the 2014–2021 time period. Colored and labelled points indicate eruption for which TADR data are available and attest a lava discharge rate decrease during the initial phase. (For interpretation of the references to colour in this figure legend, the reader is referred to the web version of this article.)

seismograms, revealing a seismic tremor composed of intermittent bursts (lasting from four to one minute) and intersected by repetitive broadband impulsive signals with LP/hybrid waveforms type (Fig. 6d). Those latter are located approximately 1 km beneath the eruptive site (Fig. 8).

4.2.2.3. Eruptive final phase and seismic gas-piston swarm. A few days later, on 22.08.2017, the usual end-of-eruption gas-piston seismic events has started to be detected, marking the final phase of the eruption (Fig. 6b). This phase lasting about five days was associated with a gradual and slow gliding of the dominant frequency observed in the spectral width on two distinct modes (Fig. 6a).
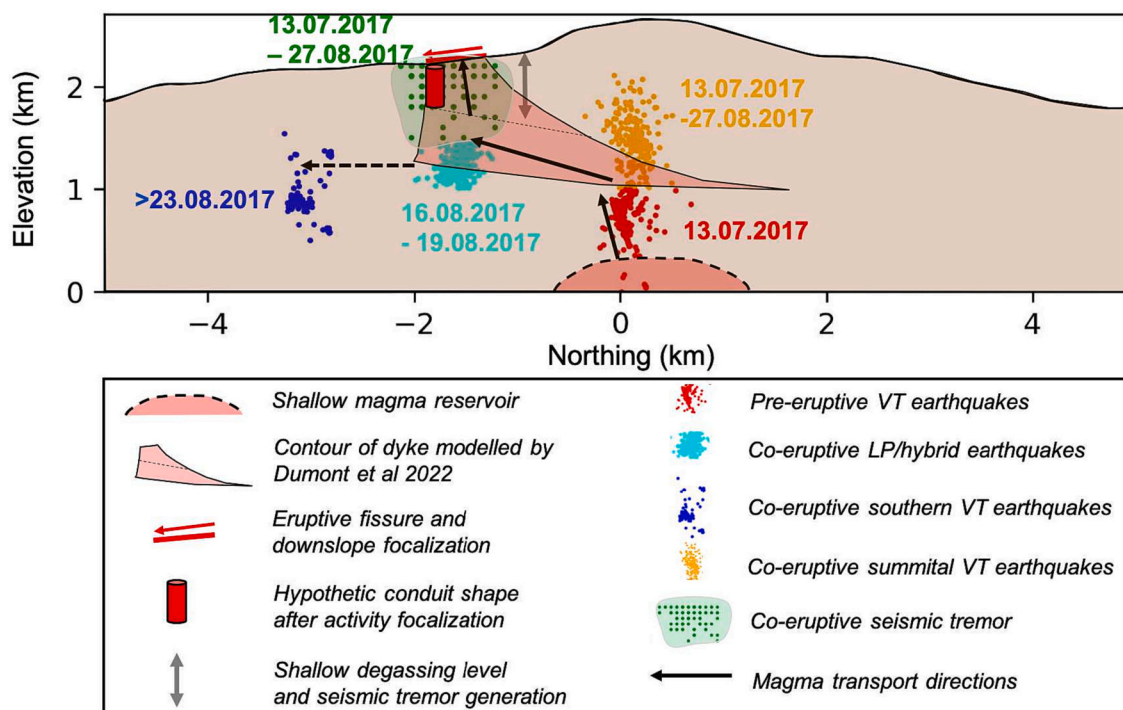
Fig. 8. Shallow magma transport and degassing with associated seismicity. Location of seismo-volcanic sources during the July–August 2017 eruption from pre-eruptive dyke propagation to co-eruptive seismic tremor. Pre-eruptive seismic swarm location is shown with red circles. The following dyke propagation is represented as the red incurved trapezoid according to Dumont et al. (2022) who inverted InSAR data to obtain this dyke geometry. The final vertical part of the dyke coincides approximately with seismic tremor sources location indicated with green circles and associated shallow degassing level. Orange circles stand for co-eruptive shallow VTs beneath the volcano summit that accommodated phase of deformation of the underlying shallow reservoir. Cyan circles represent location of LP/hybrid earthquakes taking place after an eruptive site re-feeding phase the 15.08.2017. Blue circles stand for southern VT earthquakes occurring close to the end-of-the eruption during the final phase associated with shallow gas-piston seismic events at the eruptive site. Horizontal red line represents the eruptive fissure and the above red arrow its progressive closure when eruptive activity focused in a single vent. The underlying red conduit illustrates possible shallow geometrical changes that happened following closure and cooling of shallow dyke head and explaining changes in seismic tremor properties and degassing regimes. (For interpretation of the references to colour in this figure legend, the reader is referred to the web version of this article.)

Unlike the gas-piston sequence of the short eruption of December 2020, this one is more complex and can be divided into three phases, namely, (3.1), (3.2), (3.3), indicated at the bottom of Fig. 6. We first observe in phase (3.1) the transition between the weak residual continuous tremor of the previous phase and the intermittent tremor composed of gas-piston. The increase in the number of detected multiplets of this first phase (Fig. 6b) seems to be linked to the "tremor discretization", when the seismic gas piston events become more and more individualized and are thus better detected by our template-matching method.

Then, in the phase (3.2), we observe a rapid increase in the gas-piston events recurrence frequency accompanied by a slower increase of their amplitudes (Fig. 6b). Note that those changes in gas-piston properties were accompanied by the occurrence of VTs earthquakes a few kms to the south of the eruptive site (see Fig. 6d and Fig. 8). Such seismicity might reflects the closing of the feeding dyke pushing stagnant magma further south, or a new batch of magma leaving from the shallow reservoir that did not erupt. Besides magma transport, it could also potentially be explained by stress transfer from the main magma system. This southern VT seismicity overlaps a local deformation source revealed by InSAR data (© OVPF/IPGP - August 2017 monthly bulletin, available for consultation: http://volobsis.ipgp.fr/volcano -reports/2017/08/OVPF_20170831_bullmensu.pdf).

Finally, the eruption stopped on 27.08.2017, at the end of phase (3.3), during which the number of detected gas-piston, and their amplitude, decrease until reaching the background noise level.

We provide a zoom of the spectral width function during the whole final phase in Fig. 9a, as well as examples of seismic gas-piston signals in 15-s windows in Figs. 9b-c. We can clearly observe the spectral gliding in both spectral width and gas-piston signals.

4.2.3. Explaining spectral gliding with a fluid-filled crack model

In order to better understand the origin of the observed spectral gliding, we now use the analytical equations of the resonant frequency of the rectangular fluid-filled crack derived by Maeda and Kumagai (2017) enabling to infer eruptive parameters changes as detailed in the methodological annex in the supplementary material. We decide to invert the ratio between the two observed excited modes visible in Fig. 9a (see Figs. S10 and S11) to infer possible values of the crack stiffness and crack aspect ratio (Fig. S12). We then select some of possible values in a defined range to infer the resonating crack length and its gas volume fraction by inverting the absolute values of varying frequencies of the two modes (see Figs. S13 and S14 and Table S1).

We show the results of our inversion procedure in Fig. 9c by synthesizing the different possible paths in the parameters plane "crack length" vs "gas volume fraction" that could explain the observed spectral gliding.

In all cases, the gliding is accompanied by an increase in the crack aspect ratio, which can be accommodated in different ways. Visual observations of the eruptive site indicated that in the period preceding and accompanying the transition (from 19.08.2017 to 21.08.2017) from the continuous residual tremor to the intermittent gas-piston regime, a weak effusive activity was observed over the entire width of the cone. Then, an image obtained by drone on 24.08.2017 reveals that there is only degassing on a reduced part of the cone in a "hornito" type crater of small width (probably a few meters). Thus we prefer a path not involving an increase in the width of the crack over time to explain the increase in W/L but rather a reduction in the length of the crack.

Without more external evidences, we can not determine a unique path explaining our observations, but only describe different possible
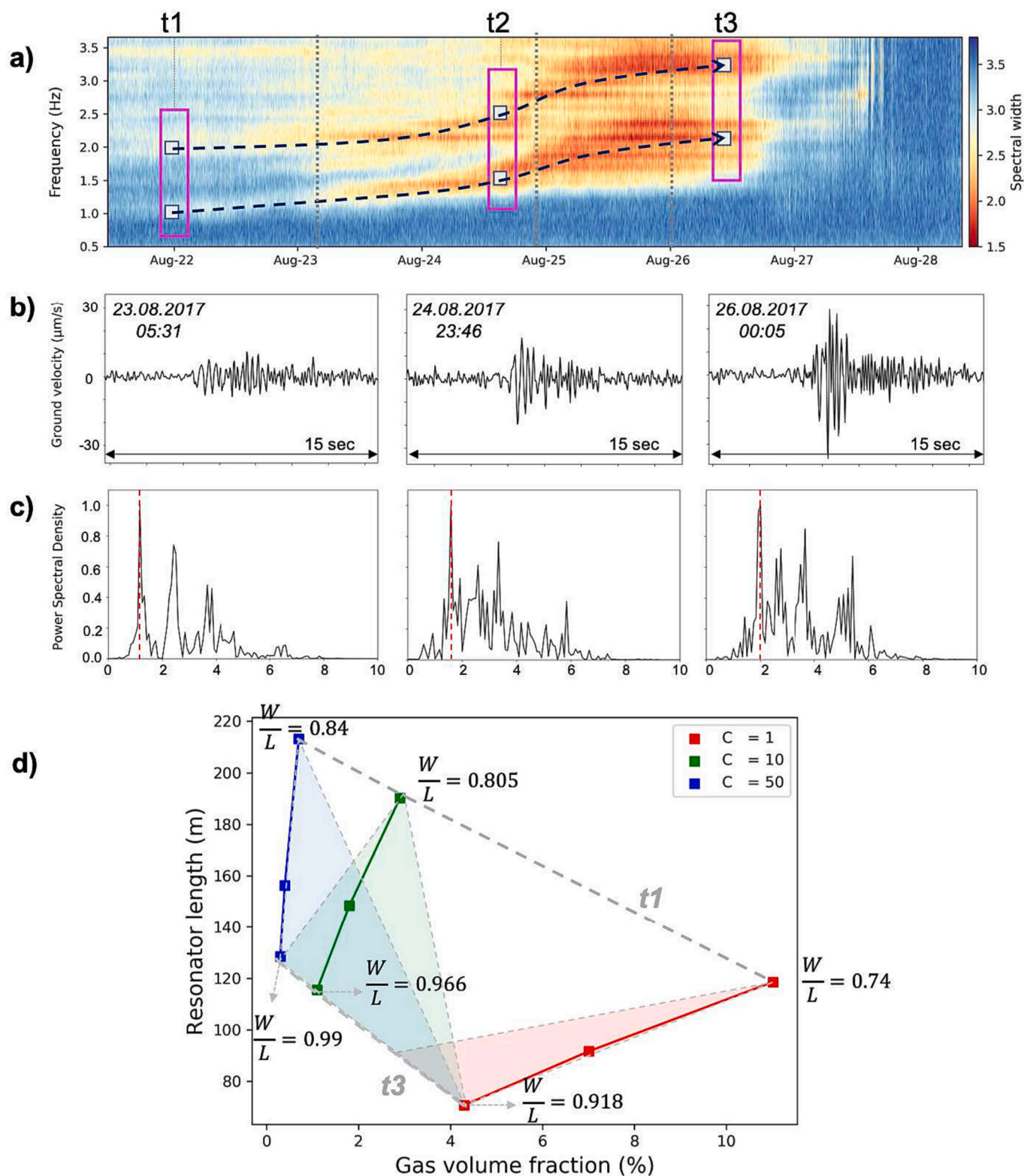
Fig. 9. Tracking seismic gas-pistons spectral changes to monitor eruptive parameters during July–August 2017 final eruptive phase. a) Zoom of the covariance matrix spectral width for the final phase of the July–August 2017 eruption. Purple rectangles indicates the time t1, t2 and t3 selected to invert observed gas-pistons frequencies (light blue rectangles) on the two activated modes highlighted with the black dashed arrows. b) and c) Examples of three seismic gas-piston event 15-s-long seismograms and corresponding spectra, respectively. Red vertical dashed lines indicate the dominant excited frequency, showing positive gliding through time. Dates of these three signals are represented with grey vertical dashed lines in a). d) Summary of possible paths explaining the observed spectral gliding in the "resonator length" vs "gas volume fraction" plane. The values obtained by setting the crack stiffness values $C = 1$, $C = 10$ and $C = 50$ are shown in red, green and blue respectively. The 2 Gy dotted lines indicate the values obtained for the date t1 of 22.08.2017 and t3 26.08.2017 12:00. The crack aspect ratio values associated with these crack stiffness values for dates t1 and t3 are indicated. (For interpretation of the references to colour in this figure legend, the reader is referred to the web version of this article.)
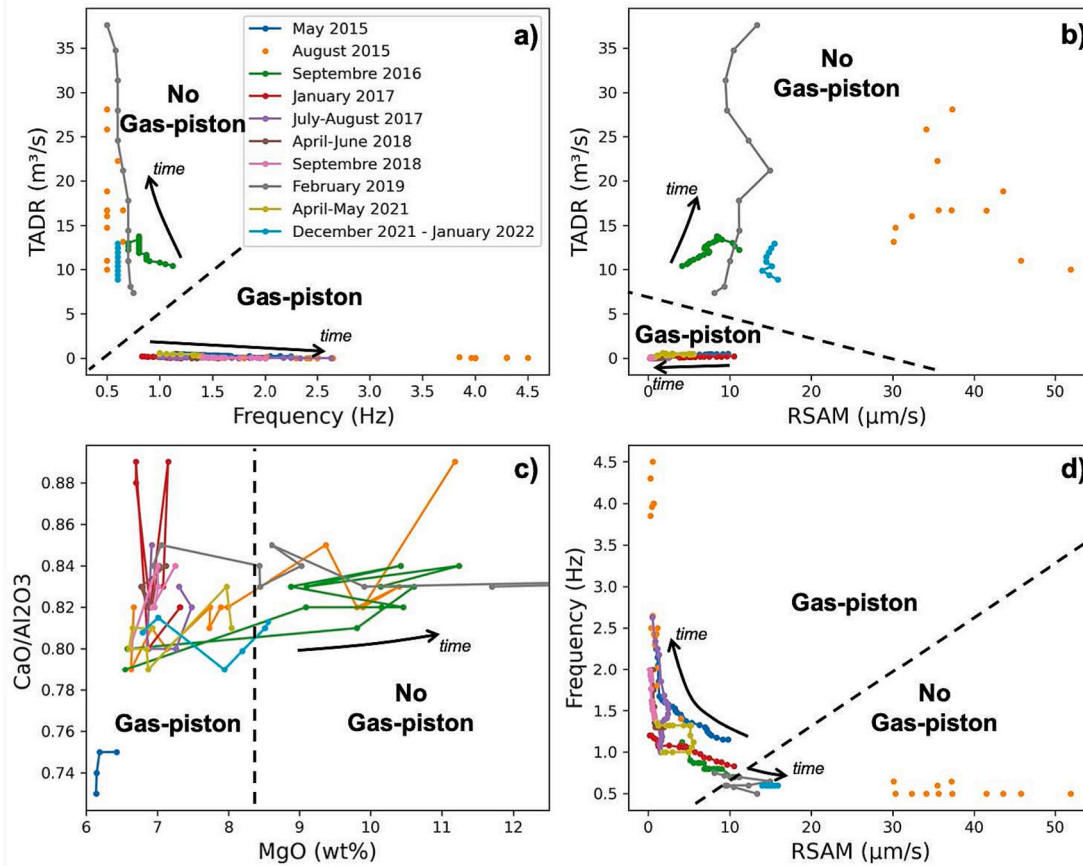
Fig. 10. Overview of Piton de la Fournaise end-of-eruption characteristics. Geophysical and geochemical measurements of ten selected final phases displayed with different colors indicated in the caption. Dashed black lines separate the final phases characterized by gas-piston swarm from the others and black arrows indicate typical time evolution of the measured parameters. a) and b) TADR as a function of the minimal excited tremor frequency and tremor RSAM, respectively. c) Ratio of CaO/Al_2O_3 as a function of the amount of MgO in wt%. d) Minimum excited tremor frequency as a function of tremor RSAM. Note that the August–October 2015 eruption is a particular case with values in both "Gas-piston" and "No Gas-piston" areas because its final eruptive phase was characterized by final effusive bursts intersected by two phases of arrest associated with gas pistoning.

scenarios. We can distinguish two extreme scenarios. The first one involves an important resonator length shortening without significant gas volume fraction changes. On the contrary, in the other one, a large part of the spectral gliding is explained by a decreasing gas volume fraction, that can be obtained by the almost complete and final degassing of the remaining magma beneath the eruptive site. Note that all intermediate paths are valid to explain our observations.

The dyke shortening can be of different nature. We can imagine a "downward dyke shortening" if the resonating bubbly lava column is drained as the magma is transported to the south flank during the VT earthquakes swarm observed in the final phase. In that case, this VT swarm could be explained by the feeding dyke closure, pushing remaining magma to the south. Another hypothesis can be that the southern magma migration is associated to a new batch of magma coming from the shallow reservoir. This might cause a re-pressurization of the shallow part of the system near the eruptive site, inducing a rise of the bubble nucleation level, and therefore an "upward shortening" of the resonant bubbly magma portion (Maryanto et al., 2008).

The observed increase in number of detected gas-piston events (Fig. 6b) can reflect a gas flux increase at the vent. This might explain the associated increase of seismic gas-piston amplitude (Spina et al., 2019). Such gas flux increase can be obtained either in the "upward shortening" case if the southern magma migration is due to a new batch of magma releasing new amount of gas beneath the eruptive site. Or it can be obtained in the case of the "downward shortening" inducing a depressurization of underlying magma with a degassing intensification. In this

latter case, we note that degassing can also be the result of stagnant magma cooling via crystallization-induced degassing.

Finally, as the observed end-of-eruption gas-piston sequence was quite long (five days) and intense, a path starting with a relatively high gas content (around 10%) might be more plausible, therefore requiring a significant drop in this gas content value through time, as inferred in Fig. 9d.

4.2.4. Gas-pistons vs effusive paroxysm: example of the February–March 2019 eruptive final phase

In this section, we provide an overview of the end-of-eruption final phases of PdF eruptions. We systematically applied our template-matching method to scan the continuous seismograms corresponding to the 23 eruptions of our catalog. We can therefore attest if their final phase is characterized by a transition from a continuous seismic tremor to a seismic gas-piston swarm or not. We indicate the presence or absence of gas-piston events in the Table 1.

From 23 eruptions, only 5 final phases are not completely associated with gas-piston events. In order to better understand the mechanisms governing degassing regime transitions leading to the end of eruptions, we compare the properties of seismic tremor in the final phases (tremor spectra, amplitude and state) with data giving insights into lava discharge rates, edifice deformation and the chemical composition of the erupted lava. We selected in total 10 eruptions (see Fig. S15) for which we have enough available data to perform our multi-disciplinary analysis.
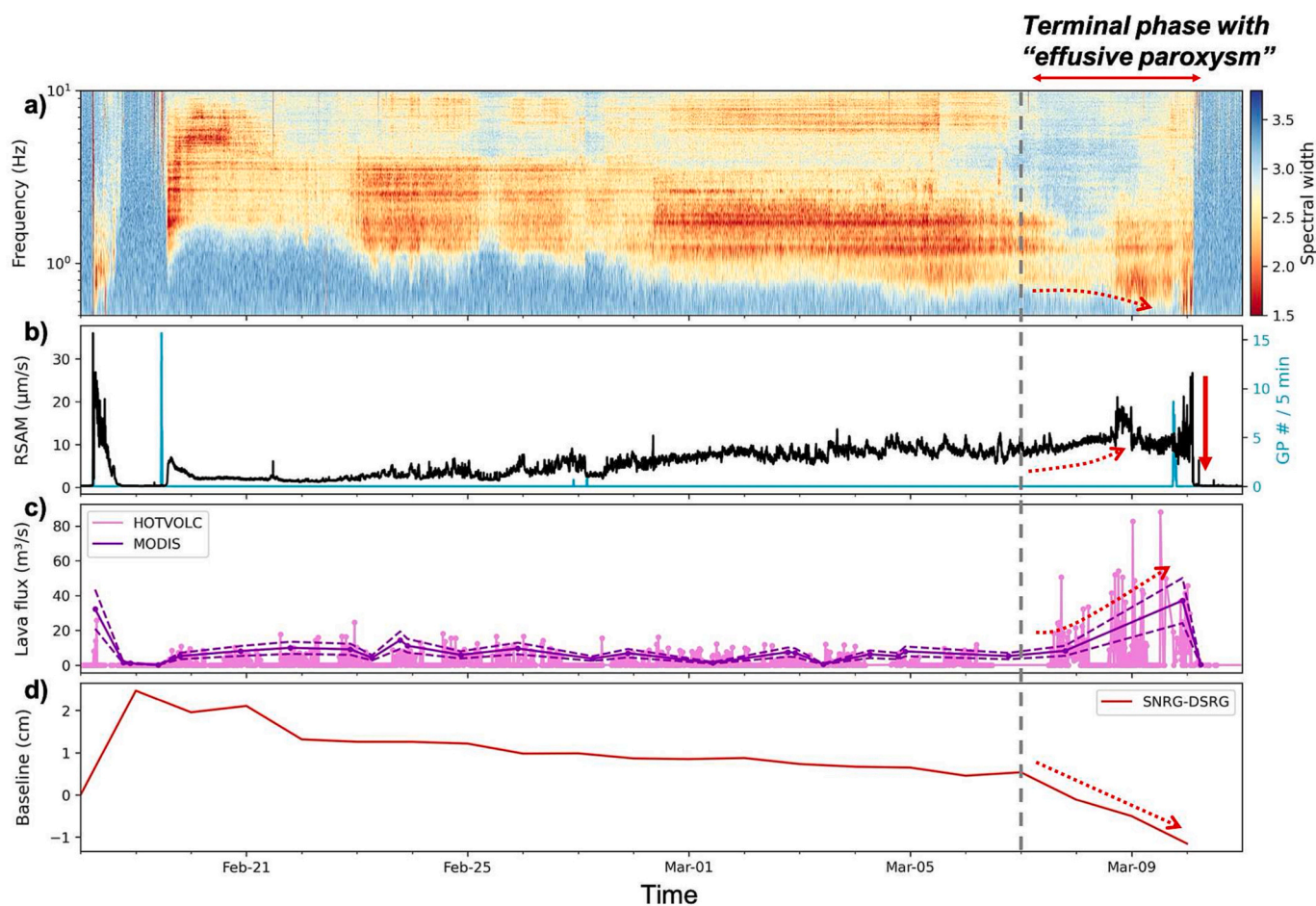
Fig. 11. Time evolution of the February–March 2019 eruption with "effusive paroxysm" during its final phase. a) Spectral width function computed in 2-min-long time windows. b) Black curve represents the tremor RSAM computed in the [0.5–5] Hz frequency band. Cyan curve indicates number of detected gas-piston event in 5 min-long time windows. c) Lava discharge rate at the eruptive vent. d) Baseline between the SNRG and DSRG summit GNSS stations. Vertical dashed grey line in a), b), c) and d) represents the start of the final eruptive phase while the red dashed arrows highlight the corresponding changes in measured parameters. Downward red arrow in b) indicates the very abrupt end of the eruption. (For interpretation of the references to colour in this figure legend, the reader is referred to the web version of this article.)

We show in Figs. 10a,b,d the resulting relationships between seismic tremor minimal excited frequency, its amplitude, and the lava discharge rate, while Fig. 10c illustrates the magma composition of the eruptions. From this database, we notice that the four eruptions not exhibiting final phase gas pistoning were characterized by larger values of TADR, magma MgO content, tremor RSAM and with activation of lower frequencies in the tremor spectra (> 1 Hz), compared to the other six eruptions with gas-pistons.

Eruptions without gas-piston are associated with a heterogeneous magma composition as seen in Fig. 10c with the increase in *MgO* content, attesting that the magma becomes more olivine-rich toward the end of the eruption, which probably indicates a deep magmatic recharge of hotter, less evolved, volatile-rich magma. Such deep magma pulses have been suggested by Coppola et al. (2017) to explain phases of "effusive paroxysm" during the August–October 2015 eruption final phase, characterized by increase in values of TADR (with return of lava fountain at the eruptive site), tremor amplitude and associated with a volcanic edifice deflation. In addition of these characteristics, we also report in Fig. S16a that these effusive paroxysms episodes are also visible in the tremor spectral content with an activation of the low frequency below 1 Hz, potentially explained by an increase of the gas volume fraction in the conduit and an increase of the length of the resonating lava column. We also note in Fig. S16b the activation of gas-piston swarm during the rest periods intersecting the three effusive paroxysm episodes.

Based on the increase in TADR and *SO₂* emissions, Verdurme et al. (2022) suggests that the final phase of the long-duration February–March 2019 eruption might also be fed by deep, volatile-rich magma. We show in Fig. 11 the temporal evolution of seismic tremor properties as well as TADR and GNSS baseline for this eruption. Besides a very brief peak in the multiplet detector function in Fig. 11b, our comparative analysis reveals that this final phase with effusive paroxysm (high TADR values in Fig. 11c) has similar characteristics than the one of August–October 2015, i.e. a low-frequency tremor activation (Fig. 11a) with high amplitude (Fig. 11b), and linked to an edifice deflation. This latter is probably induced by the emptying of the newly filled shallow reservoir by the deep magma pulse. This last magma input was then erupted during the final phase explaining the high values of TADR and magma *MgO* content.

The December 2021–January 2022 eruptive final phase was also characterized by the same parameters evolution. However, the two other eruptions not characterized by end-of-eruption gas-pistoning, namely the September 2016 and April 2020 eruptions, are not associated with a significant edifice deflation. These eruptions are shorter than the three previously mentioned ones. They lasted 6.8 days and 4.2 days, respectively, and they are both associated with irregular highly explosive behavior and TADR increase during their final phases, potentially explaining their absence of gas-piston swarm. The last day of September 2016 eruption was characterized by simultaneous Hawaiian fountaining at the main vent and transient explosive activity at a second vent (Thivet

et al., 2020b). During the two last days of the April 2020 eruption, an unusual highly explosive event occurred, with the emission of large quantities of Pele's hair (Peltier et al., 2020).

The five eruptions without gas-pistoning sequence are all characterized by a very abrupt drop in seismic tremor RSAM and eruptive activity at their end lasting a few minutes. On the contrary, the other 18 eruptions with gas-piston events are characterized by a slow decaying tremor amplitude lasting from hours to days associated to very low TADR values, probably reflecting a slow final intermittent degassing of the remaining stagnant magma beneath the eruptive site. We illustrate this tremor amplitude behavior for the end of four eruptions in Fig. S17 (eruptions June 2014 and December 2020 with the slow decaying tremor amplitude associated with gas-pistoning activity in Fig. S17a and S17c, respectively; and eruptions February–March 2019 and December 2021–January 2022 with abrupt tremor amplitude drop and without gas-pistoning activity in Fig. S17b and S17d, respectively).

5. Discussion

5.1. Shallow dyke-head magma degassing and co-eruptive tremor generation

Our co-eruptive seismic tremor signals study from the 2014–2021 period at the PdF reveals that its generation mechanism is strongly controlled by the shallow magma degassing at the head of the dyke under the eruptive site.

We shown that the tremor sources location are correlated with the strong increase of degassing at shallow depth (Fig. 3c). Those results are interesting to compare with results of shallow intrusions imaging via the inversion of InSAR data by Dumont et al. (2022). They show that eruptions away from the summit area are fed by dykes forming a spoon-shaped structure with a horizontal and vertical curvature (example in Fig. 8 for the July 2017 magma injection). This result is consistent with ours revealing that the tremor source originates at the transition where the magma transport becomes vertical a few hundred meters below the eruptive site, probably driven by the increase in buoyancy of the magma caused by its degassing.

Moreover, we also show that the initial tremor spectra seems to be controlled by the initial dyke head width arriving at the surface, of which we estimate a value by measuring the size of the eruptive fissure opened at the eruption start (Fig. 7e). The greater the fissure length, the more the initial tremor spectra is shifted toward low frequencies. Similarly, a previous study also showed that the fissure length increased with the amplitude of the tremor at PdF (Derrien, 2019).

5.2. Conduit geometry change from dyke to pipe

A few hours after the eruption start, as often observed in basaltic systems, the volcanic activity that was occurring all along the open fissure, focused in a single vent. At the PdF, this phenomenon is accompanied by a decrease in the lava flow and tremor amplitude, as well as the progressive loss of the low frequencies in the tremor spectra (Fig. 7a-d). This drop in TADR can be explained by the drop of the overpressure in the magma reservoir, when the magma is transported to the eruptive site within the dyke. This pressure drop may induce a partial closure of the dyke and focusing of volcanic activity by cooling and solidification. This surface focusing then causes a decrease in the tremor amplitude and the loss of excitation of low frequencies in its spectrum.

The spatio-temporal evolution of the fissure is governed by the thermo-rheological behavior of the magma (Bruce and Huppert, 1989) as well as the organization of the flow in the dyke (Pioli et al., 2017). This focusing process of volcanic activity represents an important phenomenon in volcanology and detailed monitoring of the co-eruptive seismic tremor properties enable to add some temporal constraints to improve its understanding.

However, the modeling of the corresponding tremor spectrum changes based on the fluid-filled crack model is complex because the focusing is also accompanied by a change in the eruptive conduit geometry from a rectangular dyke-like shape to a cylindrical pipe-like shape, the latter being mechanically and thermally more efficient for the magma transit (Fukushima et al., 2010). Also, the progressive decrease of magma gas volume fraction over time may have a role in the change in the tremor spectrum observed during the PdF initial eruptive phase.

5.3. Tracking changes in gas-liquid dynamics from measuring seismic tremor properties

The time-frequency properties of the tremor and images of the eruptive site indicate that fluctuations in the degassing regime cause changes in the tremor behavior. Tracking these changes enables monitoring the dynamics of the ongoing eruption.

5.3.1. Degassing regimes transition during short-lived eruptions

During short-lived eruptions, we show that the spectral properties and temporal stability of the tremor clearly outline in time three distinct eruptive phases (initial, intermediate and final, see Fig. 4).

The initial phase is associated with the emission of lava fountains first along the entire fissure, and then where the activity has focused to a single vent (Fig. 4 and Fig. 5).

We show in Fig. S8 that during this initial phase, although the range of values varies between eruptions, tremor RSAM and TADR seem to be coupled, both decreasing over time from an initial high value. Such RSAM/TADR coupling can be interpreted as the manifestation of a homogeneous degassing regime (Coppola et al., 2009), where gas and liquid are coupled and rise at the same speed, forming the Hawaiian degassing regimes in the conduit with corresponding lava fountains at the surface.

When the overpressure in the dyke decreases with the lava discharge rate at the vent and the dyke is not significantly replenished, the magma begins to cool, crystallize, its ascent rate slow down with increasing viscosity. Thus a decoupling between gas and liquid occurs. The bubbles have more time to coalesce and gas accumulation processes take place, marking a transition from the Hawaiian regime to a so-called Strombolian regime characterized by gas slug bursts at the surface. Thivet et al. (2020a) highlight this regime transition from the textural analysis of the eruptive products of two short PdF eruptions in June 2014 and July–August 2015. For the short December 2020 eruption, we highlight this transition from seismic tremor analysis at the beginning of the intermediate phase (Fig. 4).

The final phase is characterized by an intermittent degassing regime associated with gas-piston events. All short eruptions we analyzed between 2014 and 2021 end with a brief gas-piston swarm lasting a few hours with a decrease in the associated tremor amplitude.

The increase in viscosity and crystallinity of the nearly stagnant and highly degassed magma that resides in the dyke at the end of this type of eruption probably plays a key role in this final transition from continuous to discrete degassing/tremor. This effect was highlighted recently by Barth et al. (2019), suggesting that highly crystalline shallow portions of basaltic conduits may act as a flow valve transforming a steady gas flux into a series of discrete gas slugs.

From an analog approach through laboratories experiments in cylindrical conduits, Spina et al. (2019) reported a link between gas flux and length of slug bubbles, and that an increase in viscosity induces a longer recurrence time between slug bursts. Therefore, the reduction of gas flux and increase in magma viscosity can be associated with a decrease of bubble length and an increase of their bursting recurrence time. At some point bubbles stop bursting while the amplitude of the associated seismic events reach the background noise level. Spina et al. (2019) notes that an increase in absolute viscosity of up to two orders of magnitude is expected upon cooling and crystallization of primitive

basaltic melt from 1250 down to 1150 °C with a 3 K/min cooling rate expected in shallow dykes (Kolzenburg et al. (2016)). This could explain rapid transitions to the final gas-piston regime.

5.3.2. Complex and long-lived eruptions

Between the short and long-lived eruptions, the initial phase shows similar variations in tremor properties, except that it lasts longer in the case of the long eruptions. However, when the activity focuses on a single vent, the intermediate phase of long eruptions is more complex. This is explained as the short eruptions are fed by a single batch of magma whose evolution of temperature, viscosity, and gas content modifies the shallow gas-liquid organization, accompanied by transitions of degassing regime and associated eruptive style. On the contrary, long-duration eruptions are characterized by episodes of re-feeding during the intermediate phase, explaining their longevity.

Nevertheless, most long eruptions, after their re-feeding phases, end with a gas-piston phase. On the other hand, this last phase can be more complex than for those of short eruptions (Fig. 6 and Fig. 9).

Finally, a last possible and rarer degassing regime transition is a return to more explosive activity at the end of the eruption, reported by Coppola et al. (2017) as "effusive paroxysm" for the August–October 2015 eruption.

We report in this study similar characteristics for the end-of-eruptions of August–October 2015, February–March 2019 and December 2021–January 2022, with an increase in TADR and tremor RSAM, associated with lava fountaining, low frequency activation of tremor, eruption of slightly more mafic and phenocryst-rich magma and deflation of the volcanic edifice.

As suggested by Coppola et al. (2017) for the August–October 2015 eruption, these observations can be explained by deep magma pulses feeding these episodes of paroxysms. Such pulses can be caused by the progressive emptying and depressurization of the shallow magma reservoir during the previous eruptions. Therefore, detection and characterization of such effusive paroxysm are useful to integrate into our global knowledge of the PdF magmatic system dynamics. If final phases of the February–March 2019 and December 2021–January 2022 eruption have the same origin, this can reveal some cyclic shallow reservoir emptying.

Regarding the observation of the renewal of lava fountains at the surface during these final phases, this can be explained by an increased gas flux in the eruptive conduit (from the degassing of new deep magma), inducing longer slug bubbles, then merging and becoming an annular lava fountain regime (Spina et al., 2019).

Another characteristic of these final phases with the effusive paroxysm is that they end abruptly (tremor RSAM drop in a few minutes) compared to that with the gas-piston (tremor RSAM drop in a few hours to days). A hypothesis is that the transit of the last pulses of magma generates a significant pressure drop in the reservoir and feeding dyke, inducing a closure of the latter and a sudden end of the eruption.

6. Conclusion

We analyzed in this study the entire co-eruptive seismic tremor database available at Piton de la Fournaise between 2014 and 2021, using the covariance matrix method. The measurement of the spatial, temporal and spectral properties of the tremor informs us about its origin and its close link with the shallow magma degassing at the head of the dyke under the eruptive site. The time-frequency analysis of the tremor and its state (continuous-intermittent) combined with a multi-disciplinary study of other parameters of the system (eruptive site images, lava flow rate, deformation, magma composition) allowed us to translate the varying tremor properties into different eruptive parameters. It appears that the tremor data encodes several eruptive processes, such as volcanic activity focusing, and notable changes in degassing

regimes, at the origin of the observed fluctuations in eruptive style at the surface. Therefore, the resulting seismic database provides extremely valuable and high temporal resolution information regarding the PdF eruptive dynamics. Finally, the seismic methods used in this paper can be transposed to other basaltic systems with an adapted seismic monitoring network, thus enabling to advance in the future on a better, more global understanding of the physical mechanisms governing these eruptions and associated seismic tremor signals.

CRediT authorship contribution statement

Cyril Journeau: Conceptualization, Methodology, Software, Validation, Formal analysis, Investigation, Data curation, Writing – original draft, Writing – review & editing, Visualization. **Nikolai M. Shapiro:** Conceptualization, Methodology, Software, Validation, Investigation, Resources, Writing – original draft, Writing – review & editing, Supervision, Project administration, Funding acquisition. **Aline Peltier:** Conceptualization, Methodology, Software, Investigation, Resources, Data curation, Writing – original draft, Writing – review & editing, Supervision, Project administration. **Valérie Ferrazzini:** Conceptualization, Methodology, Software, Investigation, Data curation, Writing – review & editing. **Jean Soubestre:** Conceptualization, Methodology, Software, Validation, Investigation, Writing – review & editing. **Zacharie Duputel:** Conceptualization, Methodology, Software, Validation, Investigation, Data curation, Writing – review & editing, Visualization, Funding acquisition. **Andrea Di Muro:** Conceptualization, Methodology, Data curation, Writing – review & editing. **Claude Jaupart:** Conceptualization, Writing – review & editing. **Diego Coppola:** Data curation, Writing – review & editing.

Declaration of Competing Interest

The authors declare that they have no known competing financial interests or personal relationships that could have appeared to influence the work reported in this paper.

Data availability

Seismic data used in this study are publicly accessible via the IPGP datacenter. Other data can be made available on request.

Acknowledgements

Appendix A. Supplementary data

Supplementary data to this article can be found online at https://doi.org/10.1016/j.jvolgeores.2023.107936.

References

Bachèlery, P., 1981. Le Piton de la Fournaise (Ile de la Réunion): Etude volcanologique, structurale et pétrologique.

Ballmer, S., Wolfe, C.J., Okubo, P.G., Haney, M.M., Thurber, C.H., 2013. Ambient seismic noise interferometry in Hawai'i reveals long-range observability of volcanic tremor. Geophys. J. Int. 194, 512–523.

Barruol, G., Fontaine, F.R., 2013. Mantle flow beneath la réunion hotspot track from sks splitting. Earth Planet. Sci. Lett. 362, 108–121. https://www.sciencedirect.com/science/article/pii/S0012821X12006358. https://doi.org/10.1016/j.epsl.2012.11.017.

Barth, A., Edmonds, M., Woods, A., 2019. Valve-like dynamics of gas flow through a packed crystal mush and cyclic strombolian explosions. Sci. Rep. 9, 821. https://doi.org/10.1038/s41598-018-37013-8.

Battaglia, J., Aki, K., 2003. Location of seismic events and eruptive fissures on the Piton de la Fournaise volcano using seismic amplitudes. J. Geophys. Res. 108.

Battaglia, J., Aki, K., Staudacher, T., 2005a. Location of tremor sources and estimation of lava output using tremor source amplitude on the piton de la fournaise volcano: 2. Estimation of lava output. J. Volcanol. Geotherm. Res. 147, 291–308. https://www.sciencedirect.com/science/article/pii/S0377027305001356. https://doi.org/10.1016/j.jvolgeores.2005.04.006.

Battaglia, J., Aki, K., Ferrazzini, V., 2005b. Location of tremor sources and estimation of lava output using tremor source amplitude on the Piton de la fournaise volcano : 1. Location of tremor sources. J. Volcanol. Geotherm. Res. 147, 268–290.

Beauducel, F., Peltier, A., Villié, A., Suryanto, W., 2020. Mechanical imaging of a volcano plumbing system from gnss unsupervised modeling. Geophys. Res. Lett. 47 https://doi.org/10.1029/2020GL089419.

Bertiger, W., Bar-Sever, Y., Dorsey, A., Haines, B., Harvey, N., Hemberger, D., Heflin, M., Lu, W., Miller, M., Moore, A.W., Murphy, D., Ries, P., Romans, L., Sibois, A., Sibthorpe, A., Szilagyi, B., Vallisneri, M., Willis, P., 2020. Gipsyx/rtgx, a new tool set for space geodetic operations and research. Adv. Space Res. 66, 469–489. https://www.sciencedirect.com/science/article/pii/S0273117720302532. https://doi.org/10.1016/j.asr.2020.04.015.

Beyreuther, M., Barsch, R., Krischer, L., Megies, T., Behr, Y., Wassermann, J., 2010. ObsPy: a Python toolbox for seismology. Seismol. Res. Lett. 81, 530–533. https://doi.org/10.1785/gssrl.81.3.530 arXiv:https://pubs.geoscienceworld.org/ssa/srl/article-pdf/81/3/530/2762059/530.pdf.

Bonneville, A., 1990. Structure de la lithosphère. In: J.-F., L. (Ed.), Le volcanisme de La Réunion, monographie, pp. 1–18.

Brenguier, F., Shapiro, N.M., Campillo, M., Ferrazzini, V., Duputel, Z., Coutant, O., Nercessian, A., 2008. Towards forecasting volcanic eruptions using seismic noise. Nat. Geosci. 1, 126–130.

Bruce, P., Huppert, H., 1989. Thermal control of basaltic fissure eruptions. Nature 342, 665–667. https://doi.org/10.1038/342665a0.

Buland, R., Chapman, C.H., 1983. The computation of seismic travel times. Bull. Seismol. Soc. Am. 73, 1271–1302. https://doi.org/10.1785/BSSA0730051271 arXiv:https://pubs.geoscienceworld.org/ssa/bssa/article-pdf/73/5/1271/5331764/bssa0730051271.pdf.

Chevrel, M.O., Favalli, M., Villeneuve, N., Harris, A.J.L., Fornaciai, A., Richter, N., Derrien, A., Boissier, P., Di Muro, A., Peltier, A., 2021. Lava flow hazard map of piton de la fournaise volcano. Nat. Hazards Earth Syst. Sci. 21, 2355–2377. https://nhess.copernicus.org/articles/21/2355/2021/. https://doi.org/10.5194/nhess-21-2355-2021.

Chouet, B.A., 1996. Long-period volcano seismicity: its source and use in eruption forecasting. Nature 380, 309–316. https://doi.org/10.1038/380309a0.

Chouet, B., Dawson, P., 2011. Shallow conduit system at kilauea volcano, hawaii, revealed by seismic signals associated with degassing bursts. J. Geophys. Res. Solid Earth 116. https://doi.org/10.1029/2011JB008677.

Chouet, B., Dawson, P., 2015. Seismic source dynamics of gas-piston activity at kılauea volcano, hawai'i. J. Geophys. Res. Solid Earth 120, 2525–2560. https://doi.org/10.1002/2014JB011789.

Chouet, B.A., Matoza, R.S., 2013. A multi-decadal view of seismic methods for detecting precursors of magma movement and eruption. J. Volcanol. Geotherm. Res. 252, 108–175.

Chouet, B., Shaw, H.R., 1991. Fractal properties of tremor and gas piston events observed at kilauea volcano, hawaii. J. Geophys. Res. Solid Earth 96, 10177–10189. https://doi.org/10.1029/91JB00772.

Coppola, D., Piscopo, D., Staudacher, T., Cigolini, C., 2009. Lava discharge rate and effusive pattern at piton de la fournaise from modis data. J. Volcanol. Geotherm. Res. 184, 174–192. https://doi.org/10.1016/j.jvolgeores.2008.11.031.

Coppola, D., Di Muro, A., Peltier, A., Villeneuve, N., Ferrazzini, V., Favalli, M., Bachèlery, P., Gurioli, L., Harris, A., Moune, S., Vlastélic, I., Galle, B., Arellano, S., Aiuppa, A., 2017. Shallow system rejuvenation and magma discharge trends at piton de la fournaise volcano (la réunion island). Earth Planet. Sci. Lett. 463, 13–24. https://www.sciencedirect.com/science/article/pii/S0012821X17300365. https://doi.org/10.1016/j.epsl.2017.01.024.

Coppola, D., Laiolo, M., Cigolini, C., Massimetti, F., Delle Donne, D., Ripepe, M., Arias, H., Barsotti, S., Parra, C., Centeno, R., Cevuard, S., Chigna, G., Chun, C., Garaebiti, E., Gonzales, D., Griswold, J., Juarez, J., Lara, L., López, C., William, R., 2020. Thermal remote sensing for global volcano monitoring: Experiences from the mirova system. Front. Earth Sci. 7, 362. https://doi.org/10.3389/feart.2019.00362.

Courtillot, V., Besse, J., Vandamme, D., Montigny, R., Jaeger, J., Cappetta, H., 1986. Deccan flood basalts at the cretaceous/Tertiary boundary? Earth Planet. Sci. Lett. 80, 361–374.

Crotwell, H.P., Owens, T.J., Ritsema, J., 1999. The TauP Toolkit: Flexible Seismic Travel-time and Ray-Path Utilities. Seismol. Res. Lett. 70, 154–160. https://doi.org/10.1785/gssrl.70.2.154 arXiv:https://pubs.geoscienceworld.org/ssa/srl/article-pdf/70/2/154/2754184/srl070002_0154.pdf.

De Barros, L., Lokmer, I., Bean, C.J., O'Brien, G.S., Saccorotti, G., Métaxian, J.P., Zuccarello, L., Patanè, D., 2011. Source mechanism of long-period events recorded by a high-density seismic network during the 2008 eruption on mount etna. J. Geophys. Res. Solid Earth 116. https://doi.org/10.1029/2010JB007629.

De Barros, L., Bean, C.J., Zecevic, M., Brenguier, F., Peltier, A., 2013. Eruptive fracture location forecasts from high-frequency events on Piton de la Fournaise Volcano. Geophys. Res. Lett. 40, 4599–4603.

Derrien, A., 2019. Apports des techniques photogrammétriques à l'étude du dynamique des structures volcaniques du Piton de la Fournaise. Ph.D. thesis.. Université de Paris.

Di Muro, A., Metrich, N., Allard, P., Aiuppa, A., Burton, M., Galle, B., Staudacher, T., 2016. Magma Degassing at Piton de la Fournaise Volcano. https://doi.org/10.1007/978-3-642-31395-0_12.

Droznin, D., Shapiro, N.M., Droznina, S.Y., Senyukov, S., Chebrov, V., Gordeev, E., 2015. Detecting and locating volcanic tremors on the Klyuchevskoy group of volcanoes (Kamchatka) based on correlations of continuous seismic records. Geophys. J. Int. 203, 1001–1010.

Dumont, Q., Cayol, V., Froger, J.L., Peltier, A., 2022. 22 years of satellite imagery reveal a major destabilization structure at Piton de la Fournaise. Nat. Commun. 13, 2649. https://doi.org/10.1038/s41467-022-30109-w.

Duputel, Z., Ferrazzini, V., Brenguier, F., Shapiro, N., Campillo, M., Nercessian, A., 2009. Real time monitoring of relative velocity changes using ambient seismic noise at the piton de la fournaise volcano (la réunion) from january 2006 to june 2007. J. Volcanol. Geotherm. Res. 184, 164–173. https://www.sciencedirect.com/science/article/pii/S0377027308006239. https://doi.org/10.1016/j.jvolgeores.2008.11.024 (recent advances on the geodynamics of Piton de la Fournaise volcano).

Duputel, Z., Lengline, O., Ferrazzini, V., 2019. Constraining spatiotemporal characteristics of magma migration at Piton De La Fournaise Volcano from pre-eruptive seismicity. Geophys. Res. Lett. 46, 119–127. https://doi.org/10.1029/2018GL080895.

Endo, E.T., Murray, T., 1991. Real-time Seismic Amplitude Measurement (RSAM): a volcano monitoring and prediction tool. Bull. Volcanol. 53, 533–545. https://doi.org/10.1007/BF00298154.

Ferrazzini, V., Aki, K., Chouet, B., 1991. Characteristics of seismic waves composing hawaiian volcanic tremor and gas-piston events observed by a near-source array. J. Geophys. Res. Solid Earth 96, 6199–6209. https://doi.org/10.1029/90JB02781.

Fukushima, Y., Cayol, V., Durand, P., Massonnet, D., 2010. Evolution of magma conduits during the 1998–2000 eruptions of piton de la fournaise volcano, réunion island. J. Geophys. Res. Solid Earth 115. https://doi.org/10.1029/2009JB007023.

Goldstein, P., Chouet, B., 1994. Array measurements and modeling of sources of shallow volcanic tremor at kilauea volcano, hawaii. J. Geophys. Res. Solid Earth 99, 2637–2652. https://doi.org/10.1029/93JB02639.

Gonnermann, H.M., Manga, M., 2013. Dynamics of magma ascent in the. Modeling volcanic processes: The physics and mathematics of volcanism, 55.

Gouhier, M., Guéhenneux, Y., Labazuy, P., Cacault, P., Decriem, J., Rivet, S., 2016. HOTVOLC: a web-based monitoring system for volcanic hot spots. Geol. Soc. Lond. Spec. Publ. 426, 223–241. https://doi.org/10.1144/SP426.31.

Gurioli, L., Di Muro, A., Vlastélic, I., Moune, S., Thivet, S., Valer, M., Villeneuve, N., Boudoire, G., Peltier, A., Bachèlery, P., Ferrazzini, V., Métrich, N., Benbakkar, M., Cluzel, N., Constantin, C., Devidal, J.L., Fonquernie, C., Hénot, J.M., 2018. Integrating field, textural, and geochemical monitoring to track eruption triggers and dynamics: a case study from piton de la fournaise. Solid Earth 9, 431–455. https://se.copernicus.org/articles/9/431/2018/. https://doi.org/10.5194/se-9-431-2018.

Hibert, C., Mangeney, A., Polacci, M., Muro, A.D., Vergniolle, S., Ferrazzini, V., Peltier, A., Taisne, B., Burton, M., Dewez, T., Grandjean, G., Dupont, A., Staudacher, T., Brenguier, F., Kowalski, P., Boissier, P., Catherine, P., Lauret, F., 2015. Toward continuous quantification of lava extrusion rate: results from the multidisciplinary analysis of the 2 january 2010 eruption of piton de la fournaise volcano, la réunion. J. Geophys. Res. Solid Earth 120, 3026–3047. https://doi.org/10.1002/2014JB011769.

Houghton, B., Gonnermann, H., 2008. Explosive basaltic volcanism: constraints from deposits and models. Chemie der erde. Chem. Erde-Geochem. 68, 117–140. https://doi.org/10.1016/j.chemer.2008.04.002.

Ichihara, M., 2016. Seismic and infrasonic eruption tremors and their relation to magma discharge rate: A case study for sub-plinian events in the 2011 eruption of shinmoe-dake, Japan. Journal of Geophysical Research: Solid. Earth 121, 7101–7118. https://doi.org/10.1002/2016JB013246.

James, M., Lane, S., Chouet, B., Gilbert, J., 2004. Pressure changes associated with the ascent and bursting of gas slugs in liquid-filled vertical and inclined conduits. J. Volcanol. Geotherm. Res. 129, 61–82.

Jaupart, C., Vergniolle, S., 1988. Laboratory models of hawaiian and strombolian eruptions. Nature 331, 58–60.

Jaupart, C., Vergniolle, S., 1989. The generation and collapse of a foam layer at the roof of a basaltic magma chamber. J. Fluid Mech. 203, 347–380.

Johnson, J.B., Harris, A.J.L., Hoblitt, R.P., 2005. Thermal observations of gas pistoning at kilauea volcano. J. Geophys. Res. Solid Earth 110. https://doi.org/10.1029/2005JB003944.

Journeau, C., Shapiro, N.M., Seydoux, L., Soubestre, J., Ferrazzini, V., Peltier, A., 2020. Detection, classification, and location of seismovolcanic signals with multicomponent seismic data: Example from the piton de la fournaise volcano (la réunion, france). J. Geophys. Res. Solid Earth 125. https://doi.org/10.1029/2019JB019333 e2019JB019333.

Journeau, C., Shapiro, N.M., Seydoux, L., Soubestre, J., Koulakov, I.Y., Jakovlev, A.V., Abkadyrov, I., Gordeev, E.I., Chebrov, D.V., Droznin, D.V., Sens-Schönfelder, C.,

Journal of Volcanology and Geothermal Research 444 (2023) 107936

Luehr, B.G., Tong, F., Farge, G., Jaupart, C., 2022. Seismic tremor reveals active trans-crustal magmatic system beneath Kamchatka volcanoes. Sci. Adv. 8 https://doi.org/10.1126/sciadv.abj1571 eabj1571.

Kolzenburg, S., Giordano, D., Cimarelli, C., Dingwell, D., 2016. In situ thermal characterization of cooling/crystallizing lavas during rheology measurements and implications for lava flow emplacement. Geochim. Cosmochim. Acta 195, 244–258. https://www.sciencedirect.com/science/article/pii/S0016703716305373. https://doi.org/10.1016/j.gca.2016.09.022.

Konstantinou, K., Schlindwein, V., 2003. Nature, wavefield properties and source mechanism of volcanic tremor: a review. J. Volcanol. Geotherm. Res. 119, 161–187. https://doi.org/10.1016/S0377-0273(02)00311-6.

Lengliné, O., Duputel, Z., Ferrazzini, V., 2016. Uncovering the hidden signature of a magmatic recharge at piton de la fournaise volcano using small earthquakes. Geophys. Res. Lett. 43, 4255–4262. https://doi.org/10.1002/2016GL068383.

Lengliné, O., Duputel, Z., Okubo, P., 2021. Tracking dike propagation leading to the 2018 kĀlauea eruption. Earth Planet. Sci. Lett. 553, 116653. https://www.sciencedirect.com/science/article/pii/S0012821X20305975. https://doi.org/10.1016/j.epsl.2020.116653.

Maeda, Y., Kumagai, H., 2017. A generalized equation for the resonance frequencies of a fluid-filled crack. Geophys. J. Int. 209, ggx019. https://doi.org/10.1093/gji/ggx019.

Marchetti, E., Harris, A.J.L., 2008. Trends in activity at pu'u 'o'o during 2001-2003: insights from the continuous thermal record. Geological Society, London, Special Publications, 307, pp. 85–101. https://doi.org/10.1144/SP307.6.

Maryanto, S., Iguchi, M., Tameguri, T., 2008. Constraints on the source mechanism of harmonic tremors based on seismological, ground deformation, and visual observations at sakurajima volcano, Japan. J. Volcanol. Geotherm. Res. 170, 198–217. https://www.sciencedirect.com/science/article/pii/S0377027307003368. https://doi.org/10.1016/j.jvolgeores.2007.10.004.

Melnik, O., Lyakhovsky, V., Shapiro, N.M., Galina, N., Bergal-Kuvikas, O., 2020. Deep long period volcanic earthquakes generated by degassing of volatile-rich basaltic magmas. Nat. Commun. 11, 3918. https://doi.org/10.1038/s41467-020-17759-4.

Mordret, A., Rivet, D., Landès, M., Shapiro, N.M., 2015. Three-dimensional shear velocity anisotropic model of Piton de la fournaise volcano (La Réunion Island) from ambient seismic noise. J. Geophys. Res. Solid Earth 120, 406–427. https://doi.org/10.1002/2014JB011654.

Okada, Y., 1985. Surface deformation due to shear and tensile faults in a half-space. Bull. Seismol. Soc. Am. 75, 1135–1154. https://doi.org/10.1785/BSSA0750041135 arXiv:https://pubs.geoscienceworld.org/ssa/bssa/article-pdf/75/4/1135/5332841/bssa0750041135.pdf.

Patanè, D., Di Grazia, G., Cannata, A., Montalto, P., Boschi, E., 2008. Shallow magma pathway geometry at mt. etna volcano. Geochem. Geophys. Geosyst. 9 https://doi.org/10.1029/2008GC002131.

Peltier, A., Ferrazzini, V., Staudacher, T., Bachèlery, P., 2005. Imaging the dynamics of dyke propagation prior to the 2000-2003 flank eruptions at piton de la fournaise, Reunion island. Geophys. Res. Lett. 32 https://doi.org/10.1029/2005GL023720.

Peltier, A., Famin, V., Bachèlery, P., Cayol, V., Fukushima, Y., Staudacher, T., 2008. Cyclic magma storages and transfers at Piton de La Fournaise volcano (La Réunion hotspot) inferred from deformation and geochemical data. Earth Planet. Sci. Lett. 270, 180–188. https://doi.org/10.1016/j.epsl.2008.02.042.

Peltier, A., Ferrazzini, V., Di Muro, A., Kowalski, P., Villeneuve, N., Richter, N., Chevrel, O., Froger, J.L., Hrysiewicz, A., Gouhier, M., Coppola, D., Retailleau, L., Beauducel, F., Gurioli, L., Boissier, P., Brunet, C., Catherine, P., Fontaine, F., Lauret, F., Garavaglia, L., Lebreton, J., Canjamale, K., Desfete, N., Griot, C., Harris, A., Arellano, S., Liuzzo, M., Gurrieri, S., Ramsey, M., 2020. Volcano Crisis Management at Piton de la Fournaise (La Réunion) during the COVID-19 Lockdown. Seismol. Res. Lett. 92, 38–52. https://doi.org/10.1785/0220200212 arXiv:https://pubs.geoscienceworld.org/ssa/srl/article-pdf/92/1/38/5209738/srl-2020212.1.pdf.

Permana, T., Nishimura, T., Nakahara, H., Fujita, E., Ueda, H., 2019. Reliability evaluation of volcanic tremor source location determination using cross-correlation functions. Geophys. J. Int. 220, 1300–1315. https://doi.org/10.1093/gji/ggz523 arXiv:http://oup.prod.sis.lan/gji/article-pdf/220/2/1300/31491025/ggz523.pdf.

Pioli, L., Azzopardi, B., Bonadonna, C., Brunet, M., Kurokawa, K., A., 2017. Outgassing and eruption of basaltic magmas: the effect of conduit geometry. Geology 45 (G38787), 1. https://doi.org/10.1130/G38787.1.

Rivet, D., Brenguier, F., Clarke, D., Shapiro, N.M., Peltier, A., 2014. Long-term dynamics of piton de la fournaise volcano from 13 years of seismic velocity change measurements and gps observations. J. Geophys. Res. Solid Earth 119, 7654–7666. https://doi.org/10.1002/2014JB011307.

Rivet, D., Brenguier, F., Cappa, F., 2015. Improved detection of preeruptive seismic velocity drops at the piton de la fournaise volcano. Geophys. Res. Lett. 42, 6332–6339. https://doi.org/10.1002/2015GL064835.

Roult, G., Peltier, A., Taisne, B., Staudacher, T., Ferrazzini, V., Di Muro, A., 2012. A new comprehensive classification of the Piton de la Fournaise activity spanning the 1985-2010 period. Search and analysis of short-term precursors from a broad-band seismological station. J. Volcanol. Geotherm. Res. 241, 78–104.

Sens-Schönfelder, C., Pomponi, E., Peltier, A., 2014. Dynamics of piton de la fournaise volcano observed by passive image interferometry with multiple references. J. Volcanol. Geotherm. Res. 276, 32–45. https://www.sciencedirect.com/science/article/pii/S0377027314000596. https://doi.org/10.1016/j.jvolgeores.2014.02.012.

Seydoux, L., Shapiro, N.M., De Rosny, J., Brenguier, F., Landes, M., 2016a. Detecting seismic activity with a covariance matrix analysis of data recorded on seismic arrays. Geophys. J. Int. 204, 1430–1442.

Seydoux, L., Shapiro, N.M., de Rosny, J., Landes, M., 2016b. Spatial coherence of the seismic wavefield continuously recorded by the usarray. Geophys. Res. Lett. 43, 9644–9652. https://doi.org/10.1002/2016GL070320.

Seydoux, L., de Rosny, J., Shapiro, N.M., 2017. Pre-processing ambient noise cross-correlations with equalizing the covariance matrix eigenspectrum. Geophys. J. Int. 210, 1432–1449. https://doi.org/10.1093/gji/ggx250.

Smittarello, D., Cayol, V., Pinel, V., Peltier, A., Froger, J., Ferrazzini, V., 2019. Magma propagation at piton de la fournaise from joint inversion of Insar and gnss. J. Geophys. Res. Solid Earth 124. https://doi.org/10.1029/2018JB016856.

Soubestre, J., Shapiro, N.M., Seydoux, L., de Rosny, J., Droznin, D.V., Droznina, S.Y., Senyukov, S.L., Gordeev, E.I., 2018. Network-based detection and classification of seismovolcanic tremors: example from the Klyuchevskoy Volcanic Group in Kamchatka. J. Geophys. Res. Solid Earth 123, 564–582. https://doi.org/10.1002/2017JB014726.

Soubestre, J., Seydoux, L., Shapiro, N.M., de Rosny, J., Droznin, D.V., Droznina, S.Y., Senyukov, S.L., Gordeev, E.I., 2019. Depth migration of seismovolcanic tremor sources below the Klyuchevskoy Volcanic Group (Kamchatka) determined from a network-based analysis. Geophys. Res. Lett. 46, 8018–8030. https://doi.org/10.1029/2019GL083465.

Soubestre, J., Chouet, B., Dawson, P., 2021. Sources of volcanic tremor associated with the summit caldera collapse during the 2018 east rift eruption of kīlauea volcano, hawai'i. J. Geophys. Res. Solid Earth 126. https://doi.org/10.1029/2020JB021572 e2020JB021572. e2020JB021572 2020JB021572.

Sparks, R.S.J., 2003. Dynamics of magma degassing. Geol. Soc. Lond. Spec. Publ. 213, 22–25.

Spina, L., Cannata, A., Morgavi, D., Perugini, D., 2019. Degassing behaviour at basaltic volcanoes: New insights from experimental investigations of different conduit geometry and magma viscosity. Earth Sci. Rev. 192, 317–336. https://www.sciencedirect.com/science/article/pii/S0012825218305191. https://doi.org/10.1016/j.earscirev.2019.03.010.

Staudacher, T., Peltier, A., Ferrazzini, V., Muro, A., Boissier, P., Catherine, P., Kowalski, P., Lauret, F., Lebreton, J., 2016. Fifteen Years of Intense Eruptive Activity (1998–2013) at Piton de la Fournaise Volcano: A Review, pp. 139–170. https://doi.org/10.1007/978-3-642-31395-0_9.

Swanson, D.A., Duffield, W.A., Jackson, D.B., Peterson, D.W., 1979. Chronological Narrative of the 1969–71 mauna Ulu Eruption of Kilauea Volcano, Hawaii. https://api.semanticscholar.org/CorpusID:140711708.

Taisne, B., Brenguier, F., Shapiro, N.M., Ferrazzini, V., 2011. Imaging the dynamics of magma propagation using radiated seismic intensity. Geophys. Res. Lett. 38, 2–6. https://doi.org/10.1029/2010GL046068.

Thivet, S., Gurioli, L., Di Muro, A., 2020a. Basaltic dyke eruptions at piton de la fournaise: characterization of the eruptive products with implications for reservoir conditions, conduit processes and eruptive dynamics. Contrib. Mineral. Petrol. 175, 26. https://doi.org/10.1007/s00410-020-1664-5.

Thivet, S., Gurioli, L., Di Muro, A., Derrien, A., Ferrazzini, V., Gouhier, M., Coppola, D., Galle, B., Arellano, S., 2020b. Evidences of plug pressurization enhancing magma fragmentation during the september 2016 basaltic eruption at piton de la fournaise (la réunion island, france). Geochem. Geophys. Geosyst. 21 https://doi.org/10.1029/2019GC008611 e2019GC008611. e2019GC008611 2019GC008611.

Tsekhmistrenko, M., Sigloch, K., Hosseini, K., Barruol, G., 2021. A tree of Indo-African mantle plumes imaged by seismic tomography. Nat. Geosci. 14, 612–619.

Verdurme, P., Carn, S., Harris, A., Coppola, D., Muro, A., Arellano, S., Gurioli, L., 2022. Lava volume from remote sensing data: comparisons with reverse petrological approaches for two types of effusive eruption. Remote Sens. 14, 323. https://doi.org/10.3390/rs14020323.

Vergniolle, S., Gaudemer, Y., 2015. From Reservoirs and Conduits to the Surface. American Geophysical Union (AGU), pp. 289–321. https://doi.org/10.1002/9781118872079.ch14 chapter 14.

Vergniolle, S., Jaupart, C., 1990. Dynamics of degassing at kilauea volcano, hawaii. J. Geophys. Res. Solid Earth 95, 2793–2809. https://doi.org/10.1029/JB095iB03p02793.

Villemant, B., Boudon, G., 1998. Transition from dome-forming to plinian eruptive styles controlled by H2O and Cl degassing. Nature 392, 65–69. https://doi.org/10.1038/32144.

Vlastélic, I., Di Muro, A., Bachèlery, P., Gurioli, L., Auclair, D., Gannoun, A., 2018. Control of source fertility on the eruptive activity of piton de la fournaise volcano, la réunion. Sci. Rep. 8, 14478. https://doi.org/10.1038/s41598-018-32809-0.

Waldhauser, F., Ellsworth, W.L., 2000. A Double-Difference Earthquake Location Algorithm: Method and Application to the Northern Hayward Fault, California. Bull. Seismol. Soc. Am. 90, 1353–1368. https://doi.org/10.1785/0120000006 arXiv: https://pubs.geoscienceworld.org/ssa/bssa/article-pdf/90/6/1353/2710256/1353_ssa00006.pdf.

Walker, G.P.L., 1993. Basaltic-volcano systems. Geol. Soc. Lond. Spec. Publ. 76, 3–38. https://doi.org/10.1144/GSL.SP.1993.076.01.01.

Wamba, M.D., Montagner, J.P., Romanowicz, B., Barruol, G., 2021. Multi-mode waveform tomography of the indian ocean upper and mid-mantle around the réunion hotspot. J. Geophys. Res. Solid Earth 126. https://doi.org/10.1029/2020JB021490 e2020JB021490. e2020JB021490 2020JB021490.

Wamba, M.D., Montagner, J.P., Romanowicz, B., 2023. Imaging deep-mantle plumbing beneath la Réunion and comores hot spots: Vertical plume conduits and horizontal ponding zones. Sci. Adv. 9, eade3723 https://doi.org/10.1126/sciadv.ade3723.